Changes in Convective Available Potential Energy and Convective Inhibition under Global Warming

JIAO CHEN

School of Atmospheric Sciences, Nanjing University, Nanjing, China, and Department of Atmospheric and Environmental Sciences, University at Albany, State University of New York, Albany, New York

AIGUO DAI

Department of Atmospheric and Environmental Sciences, University at Albany, State University of New York, Albany, New York

YAOCUN ZHANG

School of Atmospheric Sciences, Nanjing University, Nanjing, China

KRISTEN L. RASMUSSEN

Department of Atmospheric Science, Colorado State University, Fort Collins, Colorado

(Manuscript received 25 June 2019, in final form 22 November 2019)

ABSTRACT

Atmospheric convective available potential energy (CAPE) is expected to increase under greenhouse gas–induced global warming, but a recent regional study also suggests enhanced convective inhibition (CIN) over land although its cause is not well understood. In this study, a global climate model is first evaluated by comparing its CAPE and CIN with reanalysis data, and then their future changes and the underlying causes are examined. The climate model reasonably captures the present-day CAPE and CIN patterns seen in the reanalysis, and projects increased CAPE almost everywhere and stronger CIN over most land under global warming. Over land, the cases or times with medium to strong CAPE or CIN would increase while cases with weak CAPE or CIN would decrease, leading to an overall strengthening in their mean values. These projected changes are confirmed by convection-permitting 4-km model simulations over the United States. The CAPE increase results mainly from increased low-level specific humidity, which leads to more latent heating and buoyancy for a lifted parcel above the level of free convection (LFC) and also a higher level of neutral buoyancy. The enhanced CIN over most land results mainly from reduced low-level relative humidity (RH), which leads to a higher lifting condensation level and a higher LFC and thus more negative buoyancy. Over tropical oceans, the near-surface RH increases slightly, leading to slight weakening of CIN. Over the subtropical eastern Pacific and Atlantic Ocean, the impact of reduced low-level atmospheric lapse rates overshadows the effect of increased specific humidity, leading to decreased CAPE.

1. Introduction

Convective available potential energy (CAPE) has been widely used to quantify atmospheric instability or the positive buoyancy that would be experienced by a lifted parcel, while convective inhibition (CIN) represents the energy needed to lift a parcel to above the level of free convection. Thus, CIN provides a measure of the stability in the lower troposphere that often prevents deep moist convection from happening if it is too strong. Both CAPE and CIN directly affect the occurrence frequency and intensity of atmospheric convection and convective precipitation. As air temperature and water vapor increase under greenhouse gas (GHG)-induced global warming, atmospheric positive buoyancy or CAPE is expected to increase, which could affect future convection and thus precipitation.

Many studies have examined model-projected future changes in CAPE under global warming, often for inferring changes in thunderstorm activities over specific

Corresponding author: Aiguo Dai, adai@albany.edu

DOI: 10.1175/JCLI-D-19-0461.1

regions (Brooks 2013; Diffenbaugh et al. 2013; Allen et al. 2014). For example, Ye et al. (1998) examined the dependence of CAPE on surface wet-bulb potential temperature and found that using CAPE variability in the current climate would overestimate the CAPE response over the tropical Pacific to 2°C surface ocean warming. Over the United States, Diffenbaugh et al. (2013) and Seeley and Romps (2015a) found robust increases in CAPE from 1970–99 to 2070–99 under RCP8.5 scenarios using CMIP5 models. CAPE and the related vertical velocity ($\sqrt{2*\text{CAPE}}$) were also found to increase over east of the Rockies from late twentieth century to late twenty-first century in other modeling studies (i.e., Del Genio et al. 2007; Trapp et al. 2007; Van Klooster and Roebber 2009; Brooks 2013). Over eastern Australia, Allen et al. (2014) found increased CAPE from 1980–2000 to 2079–99 due to increased moisture under high emissions scenarios using two global climate models. In the tropics, Seeley and Romps (2015b) found dramatically increased buoyancy in the upper troposphere and thus increased CAPE under increasing sea surface temperatures from their idealized simulations under the radiative-convective equilibrium (Romps 2014). Romps (2016) further predicted about 6%–7% increases in CAPE per 1°C surface warming of the current tropics. Other cloud-resolving simulations (Romps 2011; Muller et al. 2011; Singh and O'Gorman 2013) and global climate model simulations (Sobel and Camargo 2011) also showed increasing CAPE in response to surface warming in the tropics and other regions, including increased extreme CAPE values across the tropics and subtropics (Singh et al. 2017). The focus of these studies was often not on future CAPE changes; thus, they did not examine the global patterns and investigate the underlying processes of the CAPE increase in great detail.

Very few studies have examined model-projected changes in CIN other than that of Rasmussen et al. (2017), who showed increased CAPE and enhanced CIN (i.e., more positive and negative buoyancy) over the United States in a warmer climate using convection-permitting regional climate simulations with a 4-km grid spacing, but the exact reason for the CIN increase remains unknown. This further inspired us to look more into the CAPE and CIN changes in global climate models. Our study is also motivated by the fact that the full spectrum of atmospheric convection is affected by changes in atmospheric thermodynamic conditions such as CAPE and CIN, and thus the CAPE and CIN changes may help us explain model-simulated precipitation response to GHG-induced global warming, especially the decreases in light to moderate precipitation events (Dai et al. 2017; Rasmussen et al. 2017).

Many previous studies have examined the causes of CAPE changes. For example, Singh and O'Gorman (2013) suggested that the increase in both tropospheric saturation deficient and height of convection contribute to the increase in tropical CAPE under the assumption of radiative-convective equilibrium and zero-buoyancy approximation. Romps (2016) derived an analytical expression for CAPE (also under the assumption of radiative-convective equilibrium), which exhibits a Clausius–Clapeyron (CC) scaling and predicts increased CAPE with surface warming when the temperature is below 310 K. Some studies focused on the mechanisms for the CAPE and CIN evolution on short time scales like a few hours. For example, subsidence-induced warming was simulated to eradicate CAPE by reducing the buoyancy of the rising parcel using a two-dimensional model (Fovell 1991). Important feedbacks from downdrafts on tropospheric convective instability (i.e., CAPE) occur under convective precipitation (Emanuel et al. 1994). The response of CAPE and CIN to the thermal tendencies induced by the airflow through the modification of boundary layer growth was also studied by Parker (2002). The most intense thunderstorms on Earth occur in the vicinity of large mountain ranges such as the Andes, Rockies, and Himalayas (Zipser et al. 2006), and the primary reason is related to the thermodynamic conditions supporting deep convection. Low-level jets bring moisture into the continents, increase CAPE, and provide the necessary ingredients for convection in these regions (Carlson et al. 1983; Houze et al. 2007; Rasmussen and Houze 2016). In addition, all of these regions have a midlevel capping inversion represented by enhanced CIN that prevents the CAPE from releasing until it builds to extreme levels. This inversion is caused by heating on elevated plateaus, which forms elevated mixed layers near the Rockies and Himalayas (Carlson et al. 1983; Houze et al. 2007), and by subsidence in the lee of the Andes as the midlatitude westerlies pass over the Andes and are mechanically forced up on the windward side and down in the lee, forming a layer of adiabatically warmed air (Rasmussen and Houze 2011, 2016). Thus, CAPE and CIN are two critical thermodynamic ingredients for the formation of intense convection, and they have been examined in the context of how convection will respond to thermodynamic changes in a future climate over the United States (Rasmussen et al. 2017).

Other studies focused on the causes underlying the long-term changes in CAPE, which reflect changes in atmospheric thermodynamic conditions. CAPE changes from 1973–99 were driven mainly by the changes in low-level moisture and second by the changes in the lapse rate in selected tropical soundings (DeMott and Randall

2004). Similar results were found by Murugavel et al. (2012) over India, where increased CAPE results from increased low-level moisture and decreased upper-level temperature. The importance of near-surface moisture in explaining the CAPE variations and changes was also demonstrated in several other studies (e.g., Williams 1991; Williams and Renno 1993; Eltahir and Pal 1996; Tompkins 2001; Adams and Souza 2009). Yin et al. (2015) found that abundant low-level moisture provided by a wet surface would lower the lifting condensation level (LCL) and increase the positive buoyancy of a rising parcel, contributing to a larger CAPE in the U.S. southern Great Plains. These studies mainly revealed the important role of low-level moisture for CAPE, but few studies have investigated the factors affecting CIN besides the local inversion discussed above. The primary scientific questions addressed in this study are as follows: 1) How do low-level moisture and other factors help explain the model-projected future CAPE increases? 2) What factors would cause future CIN to become stronger?

The data and analysis method used in this study are described in section 2. Historical climatology in reanalysis data and a simple model evaluation are presented in section 3. Section 4 shows the model-projected future changes in CAPE and CIN and examines the underlying causes. A summary and discussion are given in section 5.

2. Data, model simulations, and methods

a. Data and model simulations

We used the 6-hourly data for surface pressure (PS), atmospheric temperature (T), and specific humidity (q) from historical and future simulations by the version 4 of the Community Climate System Model (CCSM4; Gent et al. 2011), which participated in the phase 5 of the Coupled Model Intercomparison Project (CMIP5; Taylor et al. 2012). These data are on 1.25° longitude × ~0.9° latitude grids, and the T and q are available vertically on a hybrid sigma pressure coordinate with a total of 26 levels. Two periods, including 1980–99 from the twentieth-century all-forcing historical simulation and 2081–2100 from the twenty-first-century simulation under the RCP8.5 high emissions scenario, were used to quantify the distributions in the historical climatology and the projected future changes under global warming. Monthly near-surface q and relative humidity (RH) data during the same periods were used to calculate their own long-term mean changes. To reduce calculations, daily PS, T, and q data for 1995–99 and 2095–99 from the same CCSM4 simulations were also used for some sensitivity tests of the different ways to calculate CAPE, CIN, and three relevant height parameters.

We also calculated CAPE and CIN using the 6-hourly ERA-Interim pressure-level data (Dee et al. 2011; ECMWF 2011) on 1° × 1° grids comparable with the CCSM4 resolution during 1980–99 to reveal the recent climatology, and to evaluate CCSM4's current climatology. ERA-Interim utilizes synoptic surface and satellite observations of air temperature and humidity (Simmons et al. 2010) and thus realistically reflects recent climatology. However, the ERA-Interim as well as other reanalyses, assimilated unhomogenized radiosonde humidity data that contain major discontinuities (Dai et al. 2011), making its humidity (and thus CAPE and CIN) trends unrealistic over many land and ocean areas (Dai et al. 2011; Byrne and O'Gorman 2018).

Moreover, the 3-hourly air pressure P, T, and q data from the high-resolution convection-permitting regional climate simulations (Liu et al. 2017) conducted at the National Center for Atmospheric Research (NCAR) Research Applications Laboratory (RAL) with the Weather Research and Forecasting (WRF) Model over North America, including the contiguous United States (CONUS), were also used for validating the CCSM4-simulated CAPE and CIN changes. The WRF-CONUS simulations cover a current 13-yr period forced by ERA-Interim data (referred to as the control or CTL run) and a future 13-yr period that includes multimodel projected mean future climate change in the ERA-Interim forcing (referred to as the pseudo global warming or PGW run). They use 4-km horizontal grid spacing and 51 vertical levels to simulate convection explicitly without cumulus parameterization, in contrast to CCSM4 and other global models. Thus, the comparison between the low-resolution CCSM4 and high-resolution WRF-CONUS results provides some evidence on whether the low-resolution CCSM4 is trustworthy for simulating future CAPE and CIN changes in comparison with high-resolution model simulations. We calculated CAPE and CIN in May–June when the near-surface warm and dry biases over the U.S. Great Plains are relatively small (Liu et al. 2017) during 2009–13 from both the CTL and PGW runs.

b. CAPE and CIN calculations

A skew T–log$p$ diagram (Fig. 1) shows the vertical profiles of air temperature and dewpoint temperature of the environment, and the areas representing CAPE and CIN for an air parcel lifted from a near-surface level. For illustrative purposes, in Fig. 1 we plotted the CCSM4-simulated 1980–99 averaged June–August (JJA) mean skew T–log$p$ diagrams for a lifted parcel under a reversible adiabatic process for a grid box centered at 40°N, 100°W over the United States and at 20°N, 140°E over the western Pacific (P1 and P2 in Fig. 4c). CAPE (in

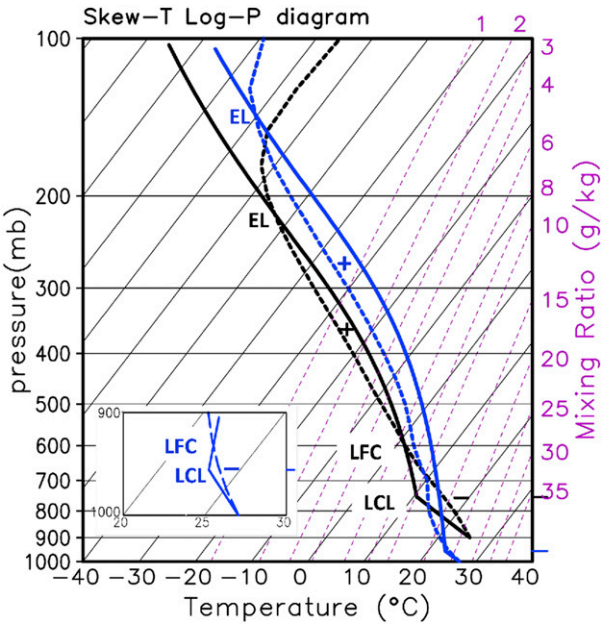

FIG. 1. The skew T–log$p$ diagram under a reversible adiabatic process with no freezing for a grid box centered at 40°N, 100°W over the United States (black lines, P1 in Fig. 4c) and 20°N, 140°E over the western Pacific (blue lines, P2 in Fig. 4c) using JJA mean temperature (T) and specific humidity (q) during 1980–99 derived using CCSM4 6-hourly data. The short-dashed lines indicate the atmospheric temperature and the solid lines indicate the parcel path lifted from the lowest level. LCL, LFC, and EL indicate, respectively, the lifting condensation level, level of free convection (the starting point of positive buoyancy, indicated by "+"), and level of neutral buoyancy (the ending point of positive buoyancy). The convective inhibition (CIN) is defined as the integral of the negative buoyancy (indicated by "−") between the lifting level and LFC while the convective available potential energy (CAPE) is defined as the integral of the positive buoyancy between LFC and EL under the reversible adiabatic process. The small inset is a blowout below 900 hPa for the ocean grid.

J kg^{-1}) is the maximum buoyancy of an undiluted air parcel integrated vertically between the level of free convection (LFC) and the level of neutral buoyancy (EL) (Fig. 1). In this study, CAPE (in J kg^{-1}) is defined as follows:

$$\mathrm{CAPE} = R_d \int_{p(\mathrm{EL})}^{p(\mathrm{LFC})} (T_{vp} - T_{ve})\, d\ln(p), \qquad (1)$$

where R_d is the gas constant of dry air and p is the air pressure. Here T_{vp} and T_{ve}, the virtual temperature of the lifted parcel and the environment respectively, are used to account for the effect of water vapor on air density (Doswell and Rasmussen 1994). Physically, CAPE describes the potential energy available for moist convection. However, a rising air parcel sometimes needs to overcome the negative buoyancy of a stable layer before reaching the LFC. The energy needed to lift an air parcel from its originating level (SFC) to the LFC (Fig. 1) is measured by CIN (in J kg^{-1}):

$$\mathrm{CIN} = R_d \int_{p(\mathrm{LFC})}^{p(\mathrm{SFC})} (T_{vp} - T_{ve})\, d\ln(p). \qquad (2)$$

These definitions of CAPE and CIN are widely recognized and consistent with many previous studies (e.g., Dai et al. 1999; Gettelman et al. 2002; Zhang 2002; Adams and Souza 2009; Riemann-Campe et al. 2009; Holley et al. 2014; Meukaleuni et al. 2016). Based on this definition of CIN, a more negative value represents an increased or enhanced CIN in this study.

The lifted air parcel will first rise dry adiabatically from the SFC to the lifting condensation level (LCL). Above the LCL, the rising parcel may follow either a reversible process (shown in Fig. 1) or an irreversible process (not shown in Fig. 1), or somewhere between these two extreme cases. The calculations for T_{vp} are different under these two assumptions (Zhang and McFarlane 1991), resulting in different values of CAPE and CIN (see appendix A for more details). CAPE under the reversible process (CAPE_r) is smaller than that under the irreversible process (CAPE_i), but they show similar distributions over the globe. These two calculation methods make little difference to our conclusions, and thus we mainly show results based on the reversible process using CAPE_r (hereafter, CAPE and CIN refer to CAPE_r and CIN_r). For the absolute stable situation with no LFC and EL (i.e., T_{vp} is always lower than T_{ve}), we define these cases as "CAPE = 0 cases" and excluded them when analyzing the CAPE and CIN changes. Moreover, we make the assumption of no freezing processes in the calculations. Although the mean CAPE and its change are substantially larger over the tropical oceans when the latent heat of fusion of ice is considered, the CAPE and CIN change patterns are very similar (see appendix B); thus the results from this study are not affected by this assumption.

CAPE values are also sensitive to the parcel level of origin [i.e., SFC in Eq. (2)] besides the various thermodynamic and microphysical assumptions (Williams and Renno 1993; Doswell and Rasmussen 1994; Emanuel 1994; Craven et al. 2002). In this study, SFC for ERA-Interim is the lowest model pressure level above Earth's surface in order to omit all pressure levels below the ground (e.g., the Tibetan Plateau). We set SFC as the lowest model level for the CCSM4 (with a hybrid-sigma value of 992.6) and WRF-CONUS (~956 hPa for the CONUS as a whole) simulations. The integration stops at the pressure level of 125 hPa for ERA-Interim, the 15th model level (with a hybrid-sigma value of 163.7) for

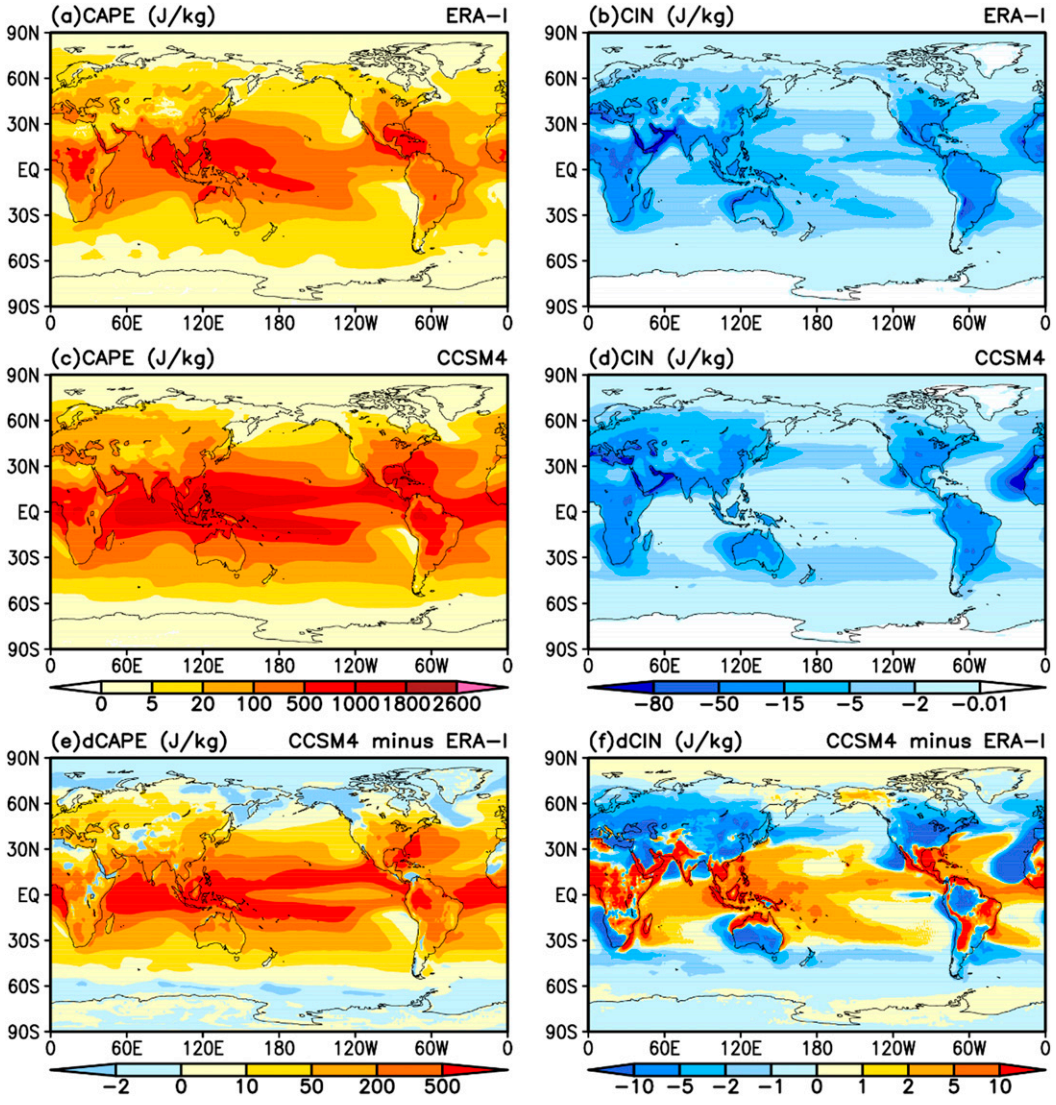

FIG. 2. Distributions of 1980–99 mean annual (left) CAPE (J kg^{-1}) and (right) CIN (J kg^{-1}) calculated under a reversible adiabatic process for a parcel lifted (a),(b) from the lowest pressure level above the ground using 6-hourly data from ERA-Interim and (c),(d) from the lowest model level with a hybrid-sigma value of 992.6 using 6-hourly data from CCSM4 historical simulation. The CAPE integration stops at the 125-hPa level for ERA-Interim and at the 15th model level (~162 hPa) for CCSM4. (e),(f) Distributions of the difference between ERA-Interim and CCSM4.

CCSM4, and the 41st model level (~125 hPa) for WRF-CONUS. Sensitivity tests using CCSM4 daily data are performed by starting and ending the parcel ascent at different levels, and are described in appendix B. Our main conclusions are insensitive to the choice of SFC and the top stopping level.

For a quantitative analysis of the three height parameters (i.e., LCL, LFC, and EL), in this study we used Espy's equation (Espy 1836; Lawrence 2005) to estimate the height of LCL. LFC and EL are simply assumed as the lowest and highest model levels with positive buoyancy in our CAPE calculations, which is sufficient for estimating their changes. Their detailed calculation methods are discussed in appendix A.

3. Recent climatology of CAPE and CIN

Before analyzing the model projected future changes in CAPE and CIN, it is helpful to first examine their climatology in recent decades. The 1980–99 mean annual CAPE decreases from over 500 J kg^{-1} in the tropics to below 5 J kg^{-1} in the polar regions (Fig. 2a). CIN is generally stronger over land than over ocean for the same latitudes (Fig. 2b), which is substantially different

from CAPE. These spatial characteristics of CAPE and CIN are consistent with the global climatology derived using ERA-40 reanalysis by Riemann-Campe et al. (2009), who noticed the strong dependency of CAPE on the near-surface specific humidity, which is also noticed in section 4.

The model-simulated CAPE (Fig. 2c) show distributions similar to those for ERA-Interim (with a pattern correlation coefficient r of 0.88) but is stronger in magnitude with a maximum over 1000 J kg^{-1} in the tropics from the Bay of Bengal to central Pacific. The CAPE difference between CCSM4 and ERA-Interim (Fig. 2e) ranges from 50 to over 500 J kg^{-1} over the tropical oceans, which may partly result from different vertical levels used in the calculations. The model-simulated CIN also shows a pattern similar to that for ERA-Interim (Fig. 2d, $r = 0.81$), but with stronger CIN over most nontropical land areas, northern South America and high-latitude oceans (especially off northwestern Africa) and weaker CIN over most low- to midlatitude oceans and some tropical land areas (Fig. 2f). The CCSM4 model can well capture the historical distribution of CAPE and CIN as compared with ERA-Interim results. Thus, it is meaningful to study the projected changes in CAPE and CIN using CCSM4 model data.

4. Model projected changes in CAPE and CIN and the underlying causes

a. CCSM4 projected changes in CAPE and CIN

The calculations of the climatology discussed in section 3 included all the so-called CAPE = 0 cases (i.e., absolute stable cases), which account for a large fraction (>60%) of all the cases in high latitudes for both ERA-Interim and CCSM4, especially during the cold season (not shown), but are seen in less than 5% for the reanalysis and 0.1% for the model of the cases over the tropical oceans (Figs. 3a,b). When the CAPE = 0 cases are excluded, the mean CAPE and CIN (not shown) over the mid- to high latitudes are enhanced but the distribution patterns over the globe are similar to Fig. 2. Thus, calculations with or without CAPE = 0 cases would not affect our general conclusions regarding the climatology in historical CAPE and CIN.

However, the annual-mean probability of CAPE = 0 cases from 1980–99 to 2081–2100 (Fig. 3c) shows widespread decreases over the Arctic and Southern Ocean and most land areas, and some increases over the eastern North Atlantic and parts of the Pacific. The decreasing probability of CAPE = 0 cases indicates more occurrences of conditionally unstable profiles in the future over the continents and high-latitude oceans. To show the projected changes in CAPE and CIN separate

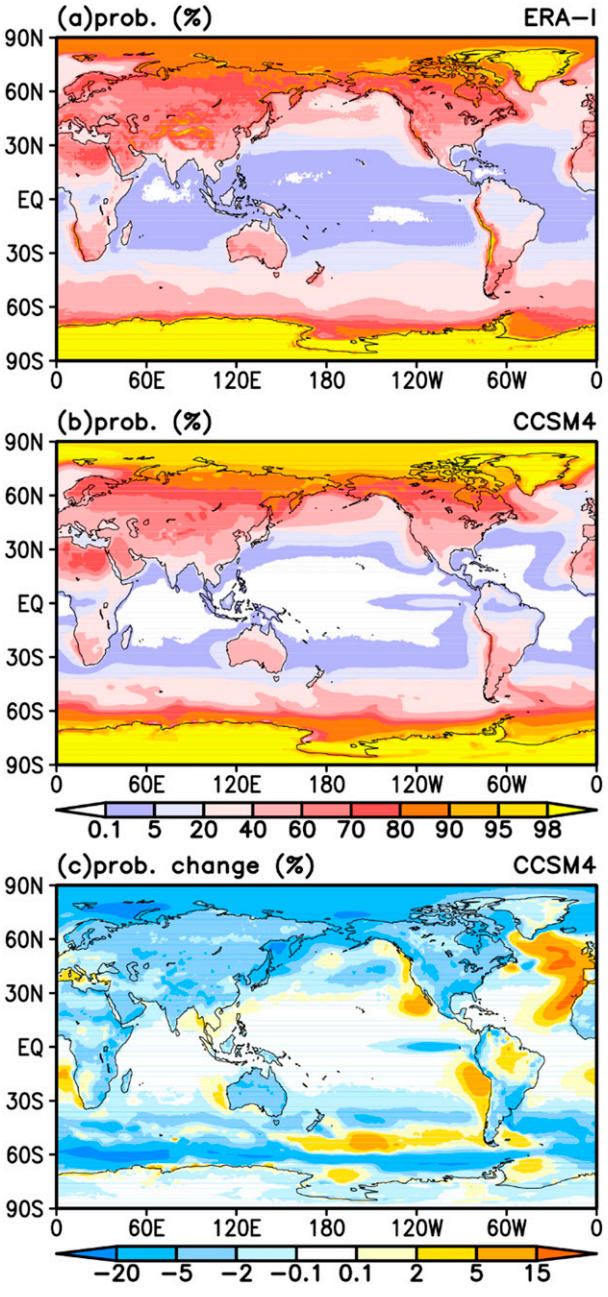

FIG. 3. Distributions of the probability (%) of CAPE = 0 cases (i.e., those absolute stable cases with the parcel temperature always lower than the environment temperature) during 1980–99 for annual mean derived using (a) ERA-Interim and (b) CCSM4 6-hourly data. (c) Changes from 1980–99 to 2081–2100 (i.e., 2081–2100 minus 1980–99, same in other figures) under the RCP8.5 scenario for CCSM4.

from these changes in the absolute stable cases, we excluded all the CAPE = 0 cases in our calculations of the future changes in CAPE and CIN discussed below.

Figure 4 shows the CCSM4-projected CAPE and CIN changes from 1980–99 to 2081–2100 under RCP8.5

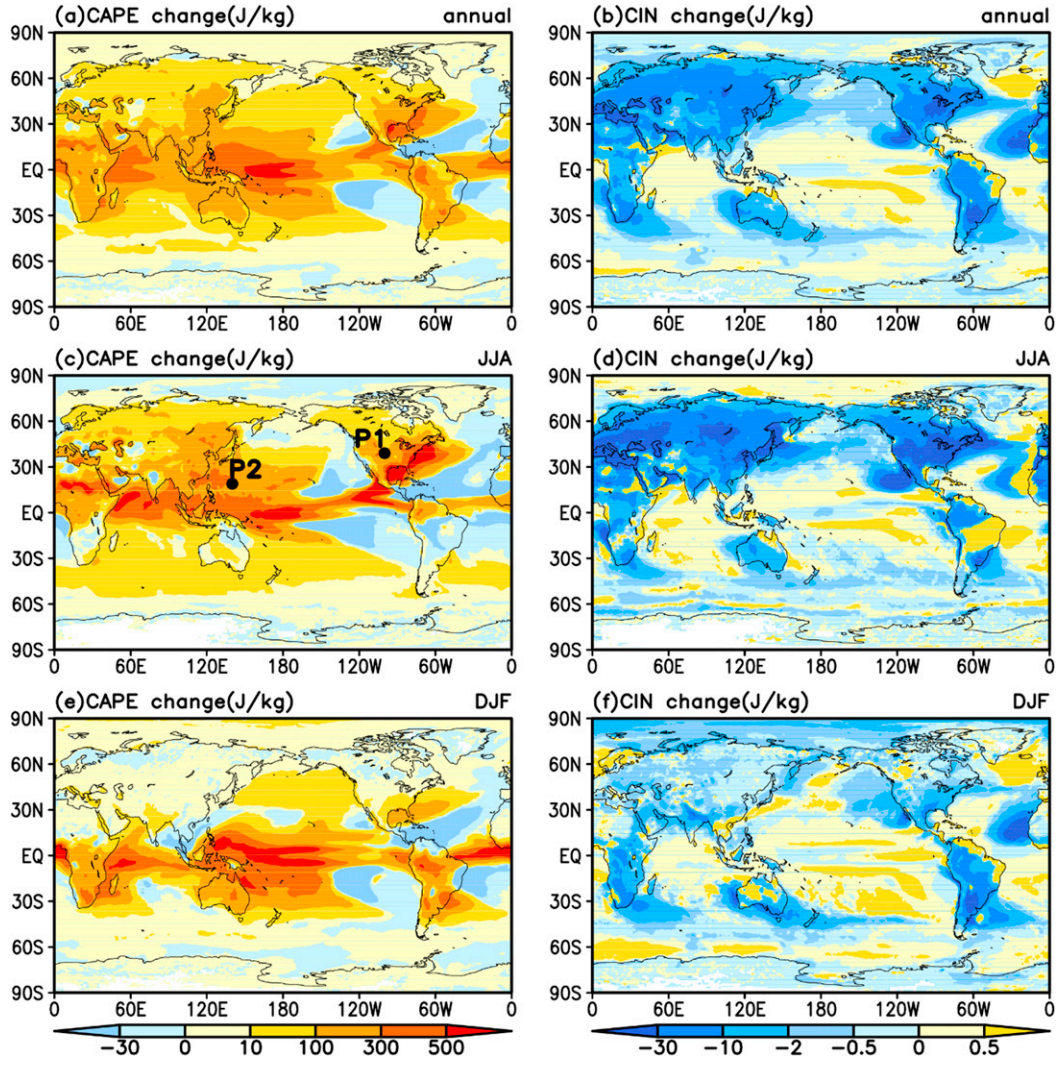

FIG. 4. Distributions of the (a),(b) annual, (c),(d) JJA, and (e),(f) DJF changes in (left) CAPE (J kg^{-1}) and (right) CIN (J kg^{-1}) from 1980–99 to 2081–2100 with the CAPE = 0 cases excluded under the RCP8.5 scenario calculated using CCSM4 6-hourly data. The CAPE and CIN with CAPE = 0 cases included also show similar change patterns. P1 and P2 in (c), centered at 40°N, 100°W and 20°N, 140°E, are two selected locations for drawing the skew T–log$p$ diagrams in Figs. 10 and 11, respectively.

scenario for annual, JJA, and DJF mean. As expected, CAPE increases over most of the globe, except the subtropical Atlantic and eastern Pacific Ocean, where it decreases slightly (Figs. 4a,c,e). Large CAPE increases are seen in the ITCZ and the western tropical Pacific and the summer continents, whereas CAPE changes little over winter continents. Surprisingly, CIN, especially over summer continents, also becomes stronger over most land areas, whereas it changes little over most oceans. In other words, both CAPE and CIN become stronger over land, especially during summer.

Qualitatively, the increases in both mean CAPE and CIN may result from more cases with large CAPE and CIN but fewer cases with small CAPE and CIN. We examine the CAPE and CIN frequency distributions and changes over different land and ocean areas using 2D histograms as a function of both CAPE and CIN (Fig. 5). Here we only show the results for summer because of the stronger CAPE and CIN in summer than in winter. Three regions including the tropics (20°S–20°N), subtropics (20°–40°S and N), and midlatitudes (40°–60°S and N) are shown. For tropical land areas, small CAPE and/or small CIN have the largest frequency and this frequency decreases with increasing CAPE and CIN (Fig. 5a). Events with small CAPE (with weak to strong CIN) or small CIN (with small-medium CAPE) are projected to decrease greatly, while events with medium-strong CAPE (with weak-medium CIN) or with medium-strong

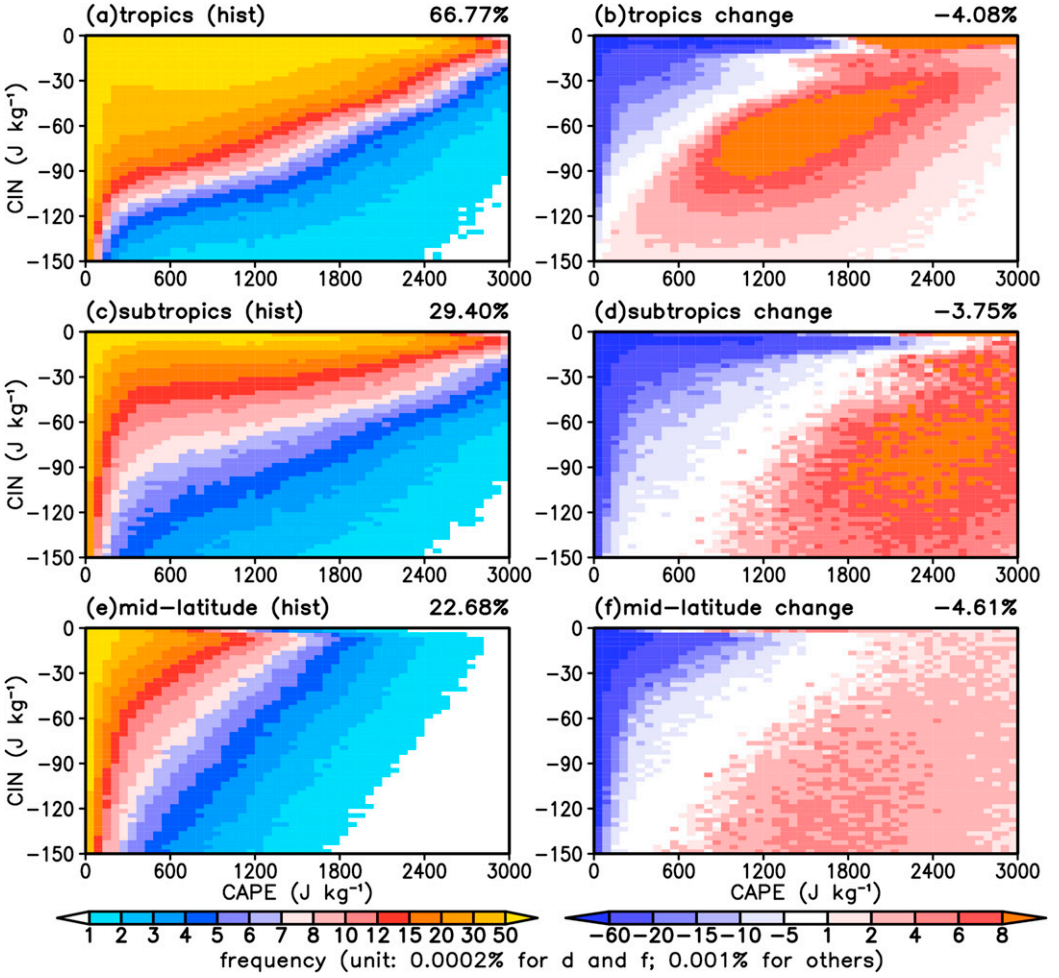

FIG. 5. (left) 1980–99 mean occurrence frequency (in % of time) of given CAPE (x axis) and CIN (y axis) values over land in different regions for summer (JJA for the Northern Hemisphere and DJF for the Southern Hemisphere), and (right) its change (in % of time) from 1980–99 to 2081–2100 calculated using 6-hourly data from CCSM4 simulations under the historical and RCP8.5 scenario. Note that the colored values need to be multiplied by 0.001 for all panels except for (d) and (f), which should be multiplied by 0.0002. The regions include the (a),(b) tropics (20°S–20°N), (c),(d) subtropics (20°–40°S/N), and (e),(f) midlatitudes (40°–60°S/N). A fixed bin number of 50 was used for both CAPE (with a bin size of 60 J kg^{-1}) and CIN (with a bin size of 3 J kg^{-1}). The total frequency or its change integrated (after the scaling) over all bins (i.e., under a limited range of CAPE and CIN, $0 < \text{CAPE} \leq 3000\ \text{J kg}^{-1}$, $-150\ \text{J kg}^{-1} \leq \text{CIN} < 0$) is shown on the top-right corner of each panel. Each pair of 6-hourly CAPE and CIN values at each grid box were taken as one occurrence and all the occurrences within the time period and geographic domain were combined to produce the frequency distributions without any averaging.

CIN (with small-medium CAPE) would increase in the future, leading to an upper-right to lower-left tilt zone of maximum frequency increases (Fig. 5b). For the subtropical and midlatitude land areas, the total occurrence frequency of CAPE and CIN are much smaller than the tropical land areas, and the ranges of CAPE are also smaller especially for the midlatitudes (Figs. 5c,e). Also, the domains of increased frequency for strong CAPE and CIN in the subtropics and midlatitudes are shifted farther toward the lower-right corner with large CAPE and strong CIN compared with the tropical case. Overall, the frequency of CAPE and CIN is projected to decrease for cases with small CAPE or CIN values but increase for cases with moderate-large CAPE and CIN values, leading to increases in the mean CAPE and CIN over land as shown in Fig. 4. These results are qualitatively similar to the results from Rasmussen et al. (2017).

The 2D frequency distributions of summer CAPE and CIN over oceans within the tropics, subtropics, and midlatitudes (Fig. 6) show noticeably different patterns for the current climatology and future changes. For example, the mean frequency of strong CIN cases is low

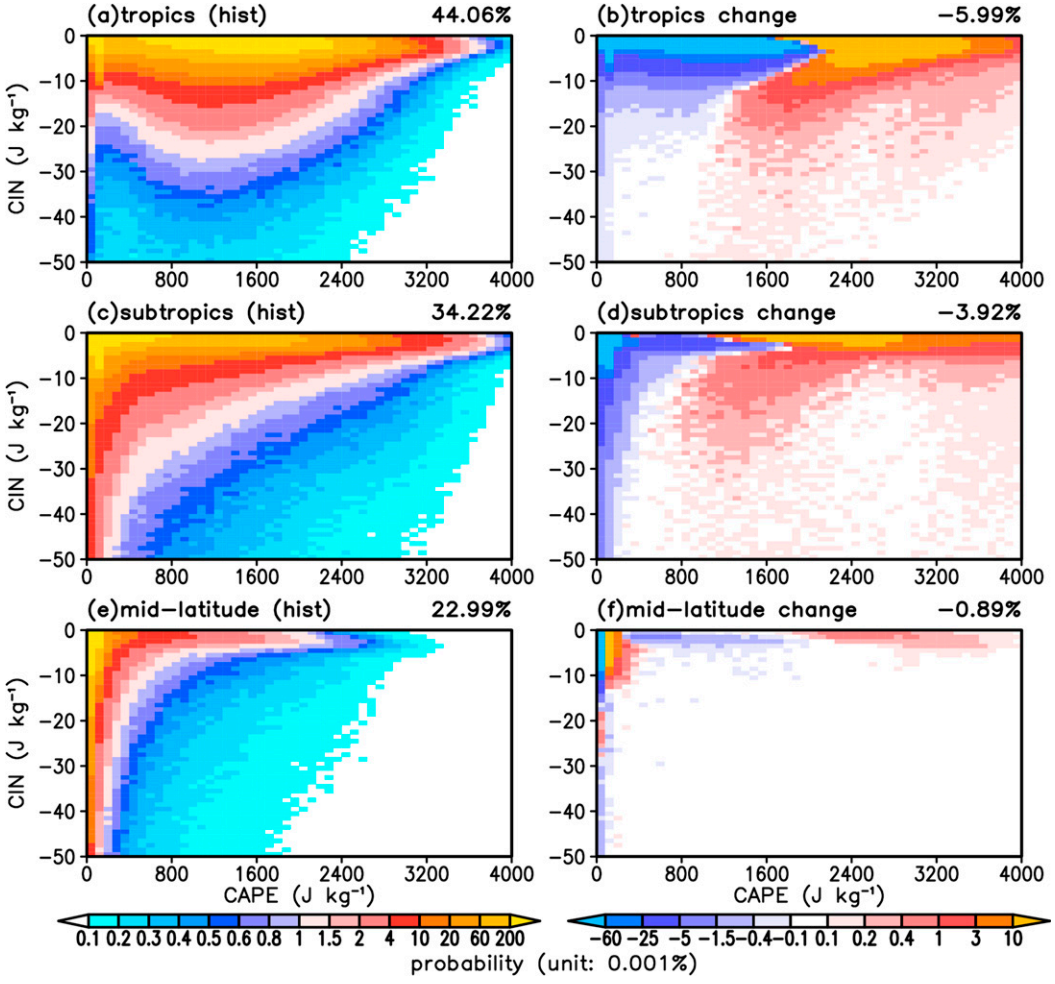

FIG. 6. As in Fig. 5, but over ocean in the three regions for a limited range of CAPE and CIN (i.e., $0 < \text{CAPE} \leq 4000\,\text{J kg}^{-1}$, $-50\,\text{J kg}^{-1} \leq \text{CIN} < 0$). Note that the colored values need to be multiplied by 0.001 for all panels. A fixed bin number of 50 was used for both CAPE (with a bin size of $80\,\text{J kg}^{-1}$) and CIN (with a bin size of $1\,\text{J kg}^{-1}$).

even when CAPE is small over tropical oceans (Fig. 6a). The decreased cases are mostly for relatively low CAPE cases, while the increased cases are mostly for relatively large CAPE cases regardless of the CIN values for the tropical and subtropical oceans (Figs. 6b,d). Such a frequency shift would lead to an increase in the mean CAPE as shown in Fig. 4. Changes are relatively small for the midlatitude oceans (Fig. 6f).

b. Comparison with WRF-CONUS simulations

Rasmussen et al. (2017) found increased CAPE and CIN downstream of the Rockies in a future warmer climate using convection-permitting high-resolution WRF-CONUS simulations, which resolve convection and individual rainstorms much better than a global model like CCSM4. Thus, a comparison between the CCSM4-simulated results and those from the WRF-CONUS should provide some evidence on the credibility of the CCSM4 in simulating future changes in CAPE and CIN. Despite the different time periods (2009–13 for current and PGW runs for WRF-CONUS; 1980–99 and 2081–2100 for CCSM4) and different approaches (PGW for WRF-CONUS and a fully coupled run for CCSM4) used in the two models, the overall change patterns should still be comparable.

The May–June mean CAPE and CIN from the WRF-CONUS control run (Figs. 7a,b) show maxima in the south-central United States and decrease northward. This pattern is similar to that seen in ERA-Interim (Figs. 2a,b) and CCSM4 (Fig. 2c,d). Their change patterns between the PGW and CTL runs (Figs. 7c,d) generally follow the distributions of their climatology, with the largest CAPE and CIN increases over the south-central United States [also shown in Rasmussen et al. (2017)]. The CCSM4 projects broadly similar CAPE and CIN change patterns from 1980–99 to 2081–2100 (Figs. 7e,f).

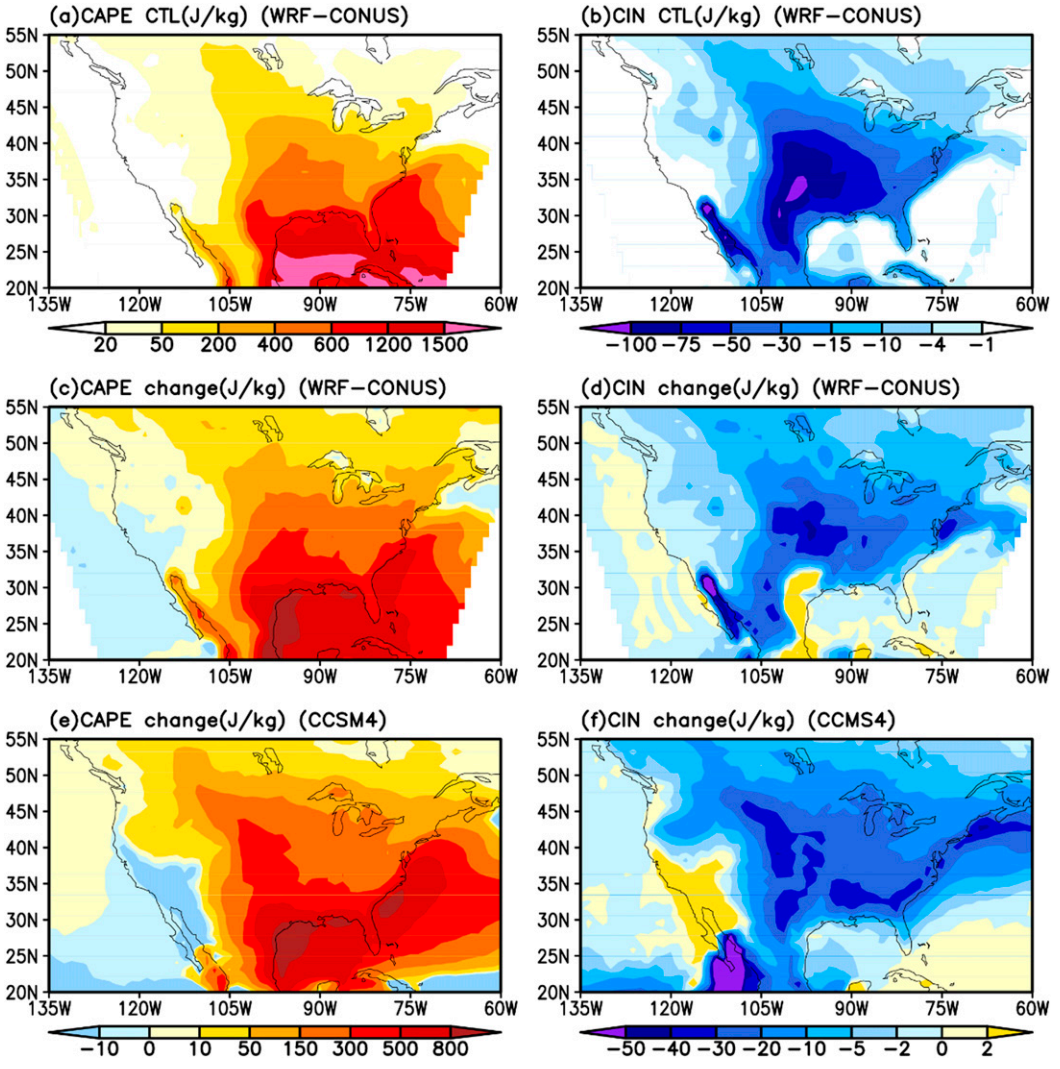

FIG. 7. Distributions of May–June mean (a) CAPE (J kg^{-1}) and (b) CIN (J kg^{-1}) during 2009–13 from the WRF 4-km control simulation (CTL) and (c),(d) the differences (J kg^{-1}) between the WRF CTL and pseudo global warming (PGW) simulation calculated using 3-hourly data from the WRF simulations. (e),(f) As in (c),(d), but using CCSM4 6-hourly data.

Thus, the CCSM4, despite of its ~1.0° grid spacing, is capable of projecting future CAPE and CIN changes seen in model simulations with convection-permitting resolution. This increases our confidence in the CCSM4-projected future thermodynamic changes.

The 2D occurrence frequency of the 3-hourly CAPE and CIN values on WRF-CONUS original model grids (not shown) is lower by a factor of about 2 than that in the CCSM4 (Fig. 8c). Averaging the WRF-CONUS CAPE and CIN data onto the CCSM4 grid increases the frequency by a factor of 2 and makes it more comparable to the CCSM4 frequency, although the frequency for low CIN and large CAPE cases and for large CAPE and large CIN cases is still lower than in CCSM4 (Figs. 8a,c). This increased frequency on larger grids is likely due to the area-aggregation effect discussed in Chen and Dai (2018); that is, the occurrence frequency or probability of a given event (e.g., precipitation, CAPE, or CIN exceeding a threshold) should increase with the area over which such an event is considered (through the averaging of the data). Results are similar when 6-hourly WRF data are used.

The WRF-CONUS simulated frequency change, after the averaging to the CCSM4 grid, is comparable to that from CCSM4, with deceased frequency for low CAPE and low CIN cases but increased frequency for high CAPE and low CIN cases (Figs. 8b,d). The main difference between WRF-CONUS and CCSM4 is that the CAPE from

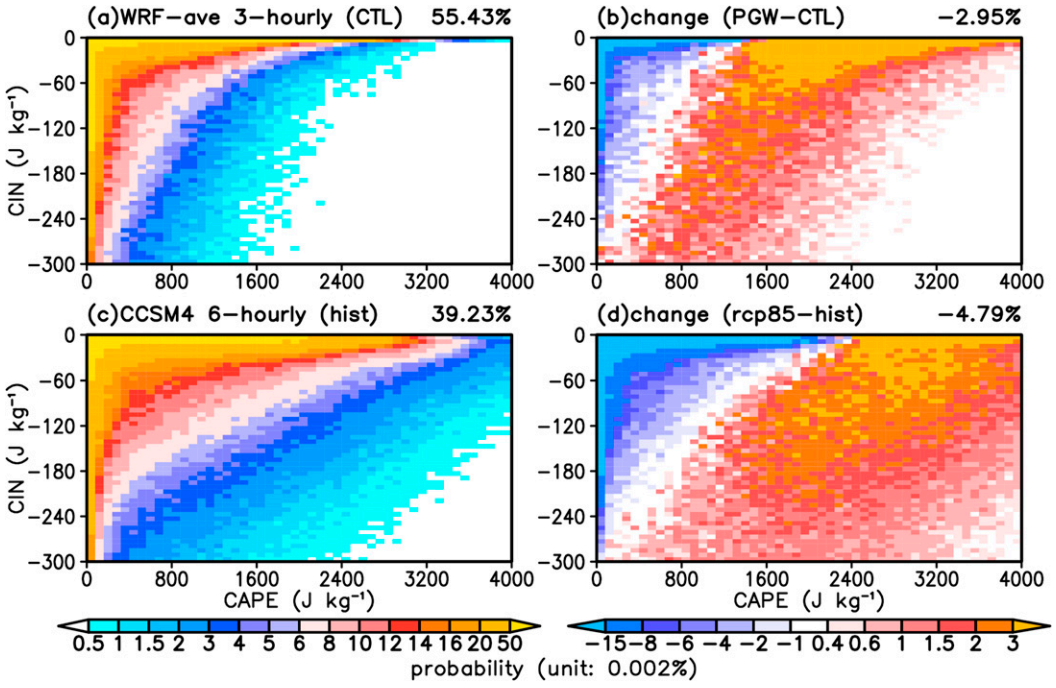

FIG. 8. (a) The occurrence frequency (in % of time) for given CAPE and CIN values in May–June during 2009–13 from the WRF control simulation (CTL) over 20°–40°N land areas of the contiguous United States (CONUS) and (b) the difference between the pseudo–global warming (PGW) and CTL simulations calculated using spatially averaged WRF 3-hourly data on the lower CCSM4 grid (i.e., simply average the high-resolution WRF CAPE and CIN data within each CCSM4 grid box). Results are similar when 6-hourly WRF data are used. (c) As in (a), but using 6-hourly data from the CCSM4 historical simulations during 1980–99. (d) The frequency change in CCSM4 from 1980–99 to 2081–2100. Note that the colored values need to be multiplied by 0.002. A fixed bin number of 50 was used for both CAPE (with a bin size of 80 J kg^{-1}) and CIN (with a bin size of 6 J kg^{-1}). The total frequency (after the scaling) integrated over all bins (i.e., under a limited range of CAPE and CIN, $0 < \text{CAPE} \leq 4000\ \text{J kg}^{-1}$, $-300\ \text{J kg}^{-1} \leq \text{CIN} < 0$) is shown on the top-right corner of each panel.

CCSM4 has a larger range, which leads to a shift toward higher CAPE values for both the climatology and the change in CCSM4 compared with WRF-CONUS.

c. *The underlying causes: The effects of increased q and decreased RH*

The definitions of CAPE and CIN [Eqs. (1) and (2)] suggest that their values are simply determined by air temperature and humidity profiles. In this subsection, we will explore how the temperature and humidity changes lead to the enhanced CAPE and CIN in the twenty-first century in CCSM4. We first did some sensitivity calculations to examine the effects of increased T and/or q on CAPE and CIN, using the 6-hourly T and q data during 1980–99 from CCSM4 historical simulation. The mean temperature increase (dT) at each grid box was defined by the 20-yr-mean T difference between 2081–2100 (under the RCP8.5 scenario) and 1980–99 (from the historical simulation). Atmospheric specific humidity (q) increases at about 7% K^{-1} under a constant relative humidity (RH; Trenberth et al. 2003). In these test calculations, q was either fixed or would increase at a rate of 7% K^{-1} or a factor of $(1 + 0.07)^{dT}$. Again, we only included the cases when CAPE is not equal to zero for the present and future CAPE and CIN calculations. Please note that these are only sensitivity tests, and they do not necessarily represent what really occurred in CCSM4.

Results show that when only T increases with q fixed, CAPE would decrease and CIN would strengthen (i.e., become more negative) over most of the globe except the high latitudes (Figs. 9a,b). This is expected because RH would decrease, which would lead to a higher LCL and LFC, leading to more CIN and less CAPE. When only q increases by 7% K^{-1} (to saturation only) with T fixed, the CAPE and CIN changes are the opposite to the T-increase only case, with increasing CAPE (especially over the tropics and extratropical land) and weakening CIN (i.e., becoming less negative) over the globe (Figs. 9c,d). This is also expected because RH would increase, which would lower the LCL and LFC, and also

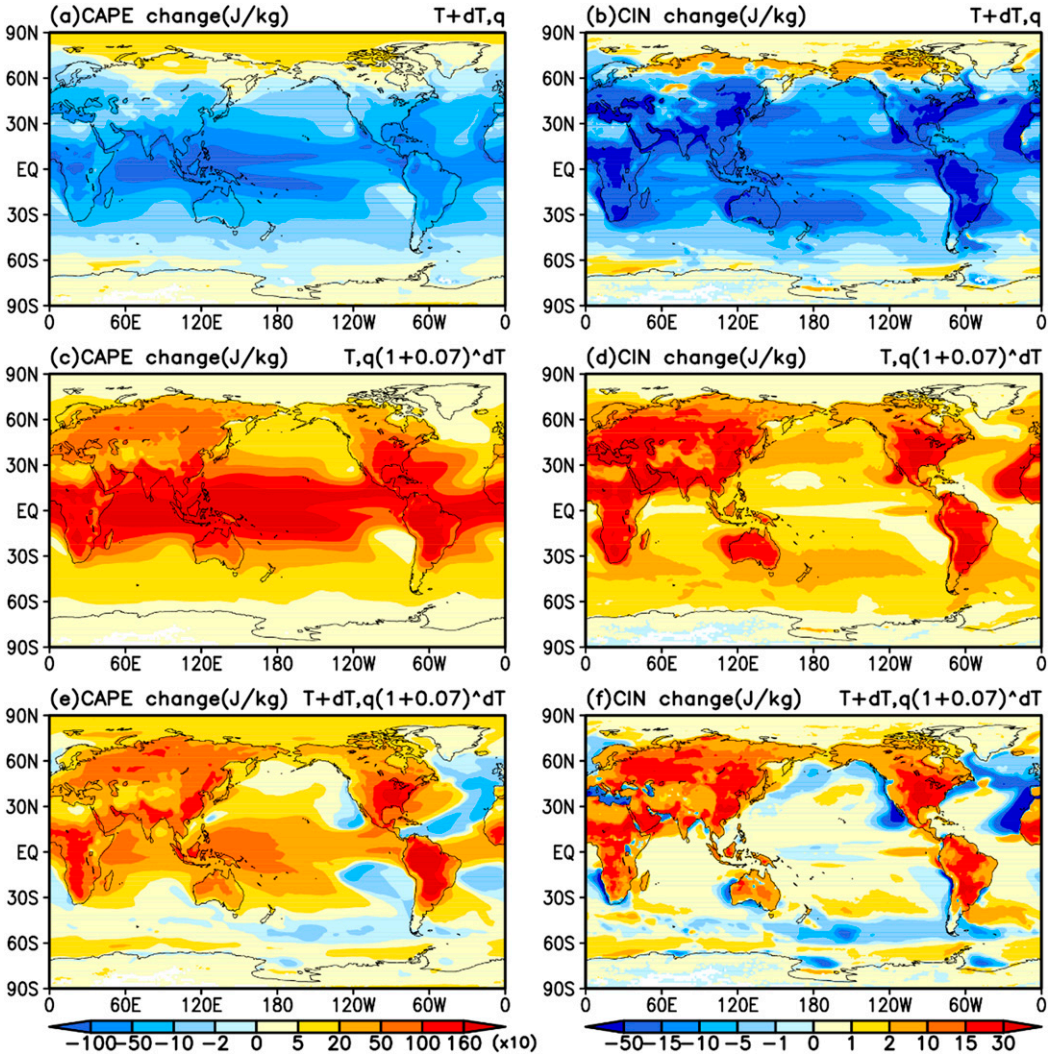

FIG. 9. As in Figs. 4a and 4b, but for the case with the future CAPE and CIN calculated using the 1980–99 6-hourly temperature (T) and specific humidity (q) data, with (a),(b) the T increase (dT) only, (c),(d) the q increase only following $q(1 + 0.07)^{dT}$, and (e),(f) both the T and q increases. The dT is the 20-yr-mean T difference between 2081–2100 and 1980–99 from the CCSM4 simulations under the historical and RCP8.5 scenarios, while the q increase rate follows that of saturation vapor pressure. Note that all the CAPE = 0 cases in the present and future periods were excluded in the calculations, and the q increase was limited by the saturation value [i.e., RH would not exceed 100% in (c) and (d)].

increase the latent heating above the LCL, leading to less CIN and more CAPE.

When both T and q increased following a constant RH, CAPE would increase over land and tropical oceans with some decreases over the subtropical eastern Pacific and Atlantic Ocean (Fig. 9e). This CAPE change pattern is comparable to that projected by CCSM4 (Fig. 4a) with a pattern correlation of 0.52, although stronger CAPE change is seen over land in Fig. 9e because low-level RH decreases slightly over land in CCSM4 as shown below. This suggests that the projected future CAPE change results mainly from the increased q approximately following a constant RH over ocean and a slightly decreased RH over land, as the T increase alone would lead to CAPE decreases. Under a constant RH, CIN would weaken over all land areas, with some strengthening over eastern subtropical oceans (Fig. 9f), in contrast to the strengthened CIN over land as projected by CCSM4 (Fig. 4b). The CIN change over oceans shown in Fig. 9f is comparable with that shown in Fig. 4b because oceanic RH does not change much in CCSM4 as shown below. Please note that while the small change in low-level RH has a large impact on CIN because the LCL, LFC, and the lapse rate of the lifted air parcel are sensitive to the RH at the lifting

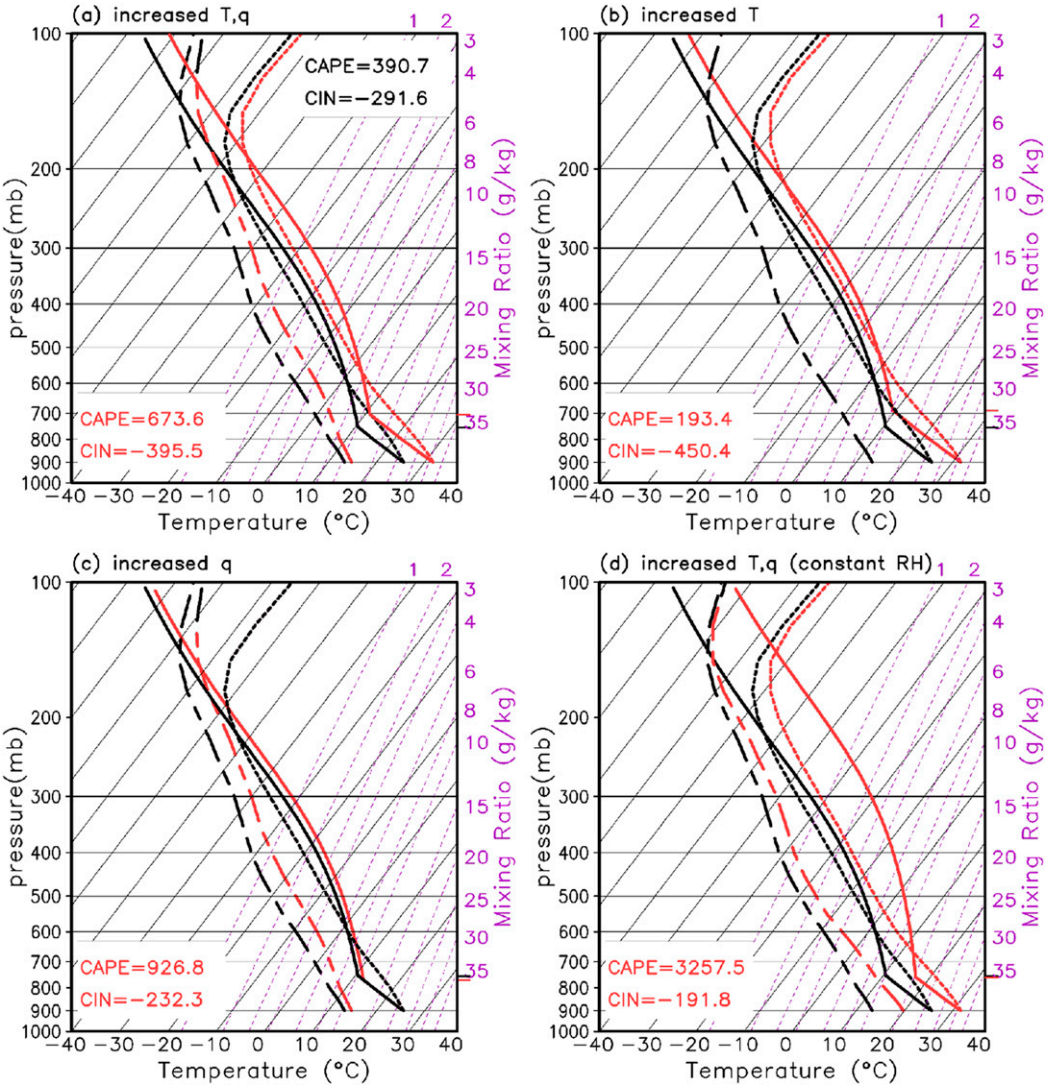

FIG. 10. (a) The skew T–log$p$ diagram under a reversible adiabatic process with no freezing for a grid box centered at 40°N, 100°W over the United States (P1 in Fig. 4c) using JJA mean temperature (T) and specific humidity (q) during 1980–99 (black lines) and 2081–2100 (red lines) using CCSM4 6-hourly data. The short-dashed and long-dashed lines indicate the atmospheric temperature and dewpoint temperature (Td) profiles, respectively, and the solid lines indicate the parcel path lifted from the lowest level. The black lines in (b)–(d) are as in (a), while the red lines correspond to the case with the CCSM4-simulated increase in (b) T only, (c) q only, and (d) the CCSM4-simulated T increase plus the q change following a constant relative humidity. The lifting condensation level (LCL) is marked by a black (for the present) or red (for the future or other tests) tick on the right-hand y axis. The CAPE and CIN values for the present are showed on the right-top corner of (a), and their values for the future or other tests are showed on the left-bottom corner of each panel.

level, the CAPE change depends heavily on the low-level q, whose change is dominated by the large T increase rather than the small RH change.

To further illustrate how the T and q changes affect CAPE and CIN, we plotted the JJA mean skew T–log$p$ diagram for a selected grid box over the central United States (Fig. 10) and another over the western Pacific Ocean (Fig. 11). For the central U.S. box, higher LCL and higher LFC in CCSM4 lead to more CIN while increased positive buoyancy above the LFC (due to increased condensation and latent heating) and higher EL lead to more CAPE (Fig. 10a). When increasing T only with q fixed, both LCL and LFC increase, leading to more CIN but less CAPE as the latent heating and EL above the LFC do not change much (Fig. 10b). When increasing q with fixed T, both LCL and LFC become lower, leading to less CIN, while the buoyancy above the LFC and the height of EL both increase, leading to much

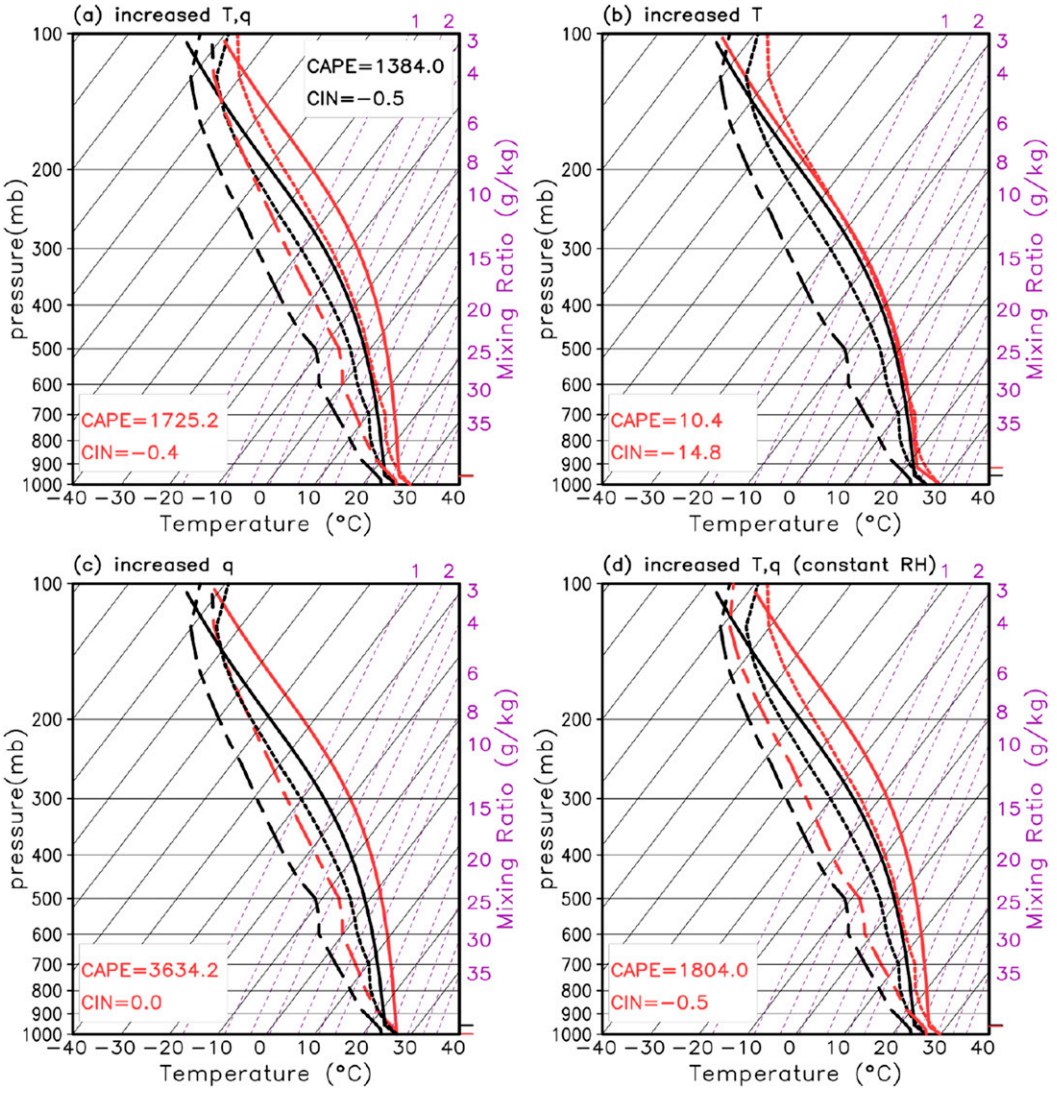

FIG. 11. As in Fig. 10, but for a grid box centered at 20°N, 140°E over the western Pacific Ocean (P2 in Fig. 4c).

larger CAPE (Fig. 10c). When both T and q increase under a constant RH, LFC move downward while LCL changes little, leading to smaller CIN; while the positive buoyancy and EL increase greatly above the LFC, leading to excessive CAPE (Fig. 10d). Thus, a constant RH under global warming would lead to lower LFC and thus less CIN over land. Figures 10a and 10d show that the constant RH assumption overestimates the humidity increase in CCSM4 mainly in the lower troposphere, where q is most important for CAPE and CIN.

Although CIN is negligible compared with the large CAPE over oceans (Fig. 2) because of the high q and low LCL, the mean skew T–log$p$ diagram still shows increased CAPE and weakened CIN under future warming (Fig. 11a). The effects of increased T or q only on CAPE and CIN for this ocean location (Figs. 11b,c) are similar to that for the land location (Figs. 10b,c). Increased CAPE is also seen under the warming with a constant RH while CIN changes little (Fig. 11d).

The above analysis indicates that increased LCL over land is related to decreased low-level RH in CCSM4. The LCL–RH relationship can also be examined from a simple theoretical analysis. The height of LCL (h_{LCL}, in units of m) can be estimated using Espy's equation as: $h_{\mathrm{LCL}} \approx 125(T - T_d)$ (Espy 1836; Lawrence 2005). Thus, h_{LCL} is proportional to the difference between air temperature T and dewpoint temperature T_d (i.e., dewpoint depression or DPD $= T - T_d$) at the lifting level, which is a measure of RH at low levels, and its change (Δh_{LCL}) is proportional to the DPD change at the lifting level. Using the Clausius–Clapeyron equation for saturation water vapor pressure: $e_s(T) = 6.11 \exp[L_v/R_v(1/273 - 1/T)]$,

we estimate the vapor pressure as $e = e_s(T_d)$ and RH = 100 e/e_s. We can further derive $\ln(100/\text{RH}) = L_v/R_v \cdot (T - T_d)/(TT_d)$ and $T - T_d = T \times T_d(R_v/L_v)(\ln 100 - \ln\text{RH})$. Since both T and T_d would increase in the future because of the increased T and q, decreasing RH would lead to increasing $T - T_d$, and thus increasing h_{LCL} (Fig. 10a). When RH is fixed, h_{LCL} increases only slightly due to the small fractional increase in $T - T_d$, and CIN weakens mainly because of the decreased level of LFC, which results from a smaller moist adiabatic lapse rate (γ_m) under higher T and q in the future, as γ_m decreases with air temperature (see below). Myoung and Nielsen-Gammon (2010) indicated that the difference between the lower tropospheric temperature and near-surface dewpoint temperature is a good proxy of CIN. From our analysis, we can see this approximate relationship results from the change of LCL.

Above the LCL, γ_m of the lifted air parcel can be derived as (Wallace and Hobbs 1977): $\gamma_m = -dT/dz = \gamma_d + (L_v/c_{\text{pd}}) \times (dr_s/dz)$, where γ_d is dry adiabatic lapse rate; the saturation mixing ratio $r_s = \varepsilon \times e_s/(p - e_s) \approx \varepsilon \times e_s/p$ and $dr_s/dz \approx \varepsilon \cdot (de_s/dz)/p$ represents the vapor loss rate, where c_{pd} is the specific heat of dry air at constant pressure and $\varepsilon(\approx 0.622)$ is the ratio of the gas constants of air and water vapor. Note that e_s and r_s increase with T and dr_s/dz becomes more negative (i.e., decreases faster with height) in a warmer climate; thus, γ_m is smaller in a warmer climate. Physically, this is because of the increased condensation and latent heating above the LFC as q increases in the future, which slows down the cooling as the parcel ascends. This would shift the parcel moist adiabat to the right (thus more positive buoyancy) and ensure a smaller γ_m and thus a higher EL (Fig. 10a). Without the increased q, the γ_m would not change much and the EL would be similar, and CAPE would decrease because of the increased LCL and LFC (Fig. 10b).

To further demonstrate the importance of increased q to the CAPE change over the globe and the role of reduced RH for the enhanced CIN over land, in Fig. 12 we show the annual, JJA, and DJF mean changes in near-surface q and RH. The near-surface q is projected to increase everywhere over the globe with the largest increases in the tropics and in the summer hemisphere (Figs. 12a,c,e). The q change patterns are broadly consistent with the CAPE change patterns (Fig. 4) and their pattern correlation coefficients are 0.70, 0.62, and 0.69 for annual, JJA, and DJF, respectively, which implies a strong relationship between the near-surface q and CAPE changes. In contrast, the near-surface RH would decrease over most land areas but increase over most oceans, especially over summer Northern Hemisphere land (Figs. 12b,d,f). These RH change patterns are broadly comparable with the CIN change patterns shown in Fig. 4, except for some areas over the North Pacific and North Atlantic where increased RH and enhanced CIN are seen. Their pattern correlation coefficients over all the land grid points are 0.25, 0.30, and 0.20 for annual, JJA, and DJF, respectively. Thus, while q is increased globally under global warming, its increase over the continents is not enough for maintaining a constant RH, which increases surface water vapor deficit and contributes to surface drying over land under global warming (Dai et al. 2018). The increased q would lead to more condensation and latent heating above the LFC, smaller moist lapse rate for the lifted parcel, and higher EL and thus more CAPE over the globe, except for some subtropical oceans which are discussed in section 4d. On the other hand, the decreased RH over land would raise the LCL and LFC (Fig. 10a) and result in enhanced CIN, while increased RH over oceans would slightly weaken CIN there.

The near-surface q and RH changes can affect LCL, LFC, and EL and thus CAPE and CIN over the globe. The mean LCL during 1995–99 is much higher over land than over ocean although low LCL is also seen over tropical Africa, South America, and Southeast Asia (Fig. 13a) and would increase over most land areas and decrease over most oceans from 1995–99 to 2095–99 (Fig. 13b). The LFC generally follows the distribution of the LCL (but with low LFC over many subtropical and equatorial oceans) and is also projected to increase over most land areas and decrease over most oceans (Figs. 13c,d). The higher levels of LCL and LFC in the future enhance CIN but decrease CAPE over most land areas (see appendix C). The distribution of EL (Fig. 13e) is comparable with the distributions of CAPE (Fig. 2c), with high levels over the tropical land and oceans and low levels over subtropical oceans and mid- to high latitudes. EL would increase and contribute to the increased CAPE in the future over most of the globe except the subtropical oceans (Fig. 13f).

As explained in appendix C, a precise calculation of the contributions by these individual factors is impossible because of the dependence of the LCL, LFC, and EL on the T and q profiles and thus the lapse rates. Our estimates (see Fig. C1 in appendix C) using the current and future mean T and q profiles suggest that most (>60%) of the CAPE change results from lapse rate changes of both the environment and the ascending parcel, while the EL change contributes about 20%–40% of the CAPE change over most of the globe. The increased LFC leads to 1%–5% reduction in CAPE over most land but contributes little over the oceans. Similarly, most (>80%) of the CIN changes result from lapse rate changes, with the LFC change contributing only about 5%–20% to the CIN strengthening over land (Fig. C2).

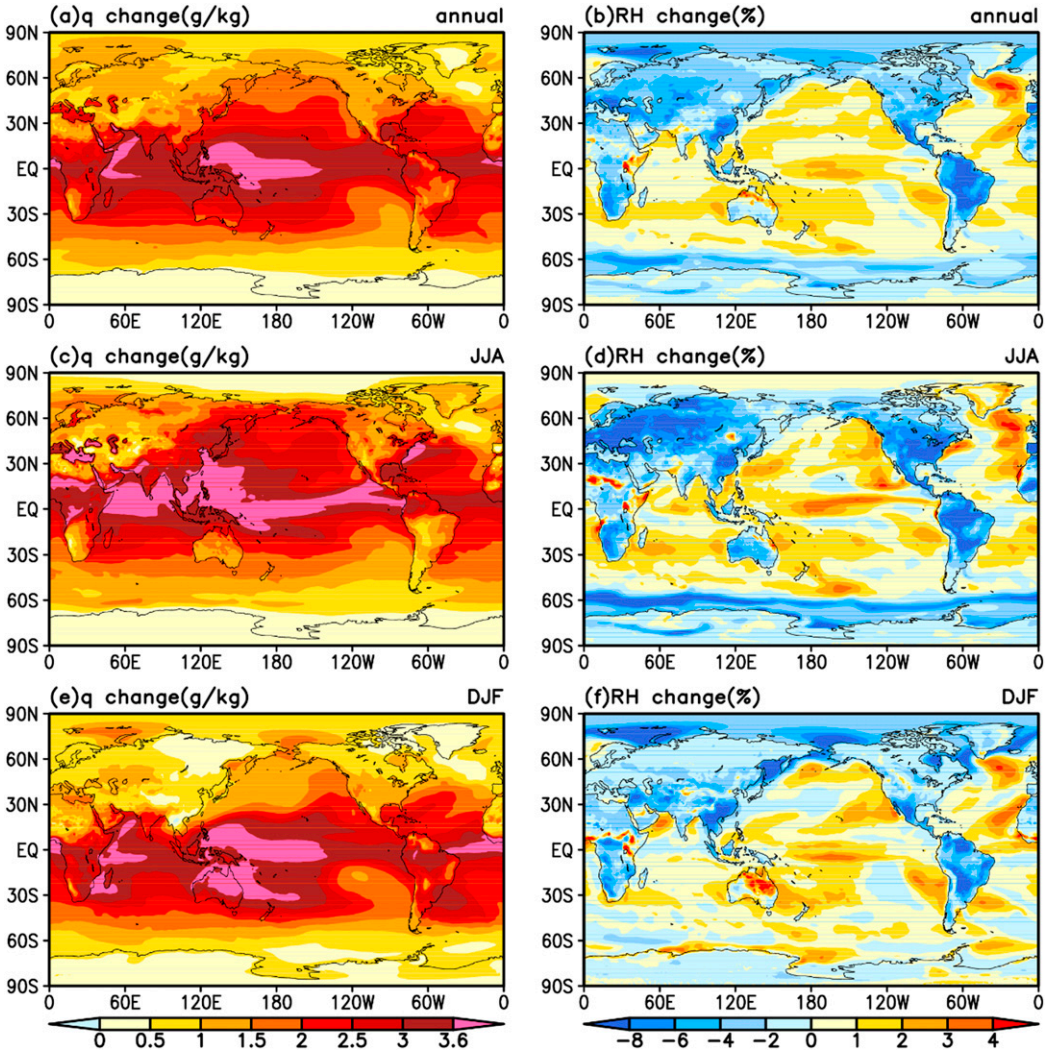

FIG. 12. Changes in (left) near-surface specific humidity (q; g kg^{-1}) and (right) near-surface relative humidity (RH; %) from 1980–99 to 2081–2100 for the (a),(b) annual, (c),(d) JJA, and (e),(f) DJF means under the RCP8.5 scenario using CCSM4 monthly data.

d. Effects of atmospheric lapse rates

Besides the moisture content of the lifted air parcel, which affects the lapse rate of the ascending parcel, the value of CAPE is also affected by the atmospheric lapse rate (i.e., the lapse rate of the environment; see Fig. 1), which is considered as a secondary driving factor besides low-level moisture in tropics by DeMott and Randall (2004). The changes in atmospheric lapse rates may help explain the decreased CAPE in a future warmer climate over the subtropical eastern Pacific and Atlantic (Fig. 4). Annual-mean skew T–log$p$ diagrams using CCSM4 daily data (not shown) revealed weakening atmospheric lapse rates around 800 hPa over these subtropical oceans, which may be more than enough to offset the CAPE increase from increased q as the LCL is usually lower than 900 hPa over oceans. The air temperature difference between the 1st (around 978.1 hPa) and 5th (around 776.4 hPa) level can provide a measure of the atmospheric lapse rate in the lower troposphere (Fig. 14a). Simulated changes in this measure show largest decreases over the subtropical oceans (for reasons not well understood), where CAPE decreases (Figs. 14b and 4a). This effect appears to overwhelm the positive contribution from increased q (which is relatively small over the subtropical oceans) to the CAPE increase, leading to CAPE decreases there. The atmospheric lapse rate change (Fig. 14b) is small over other ocean areas (except the Arctic Ocean where sea ice loss–induced warming decreases with height; Dai et al. 2019), and the effect of increased q dominates, leading to CAPE increases.

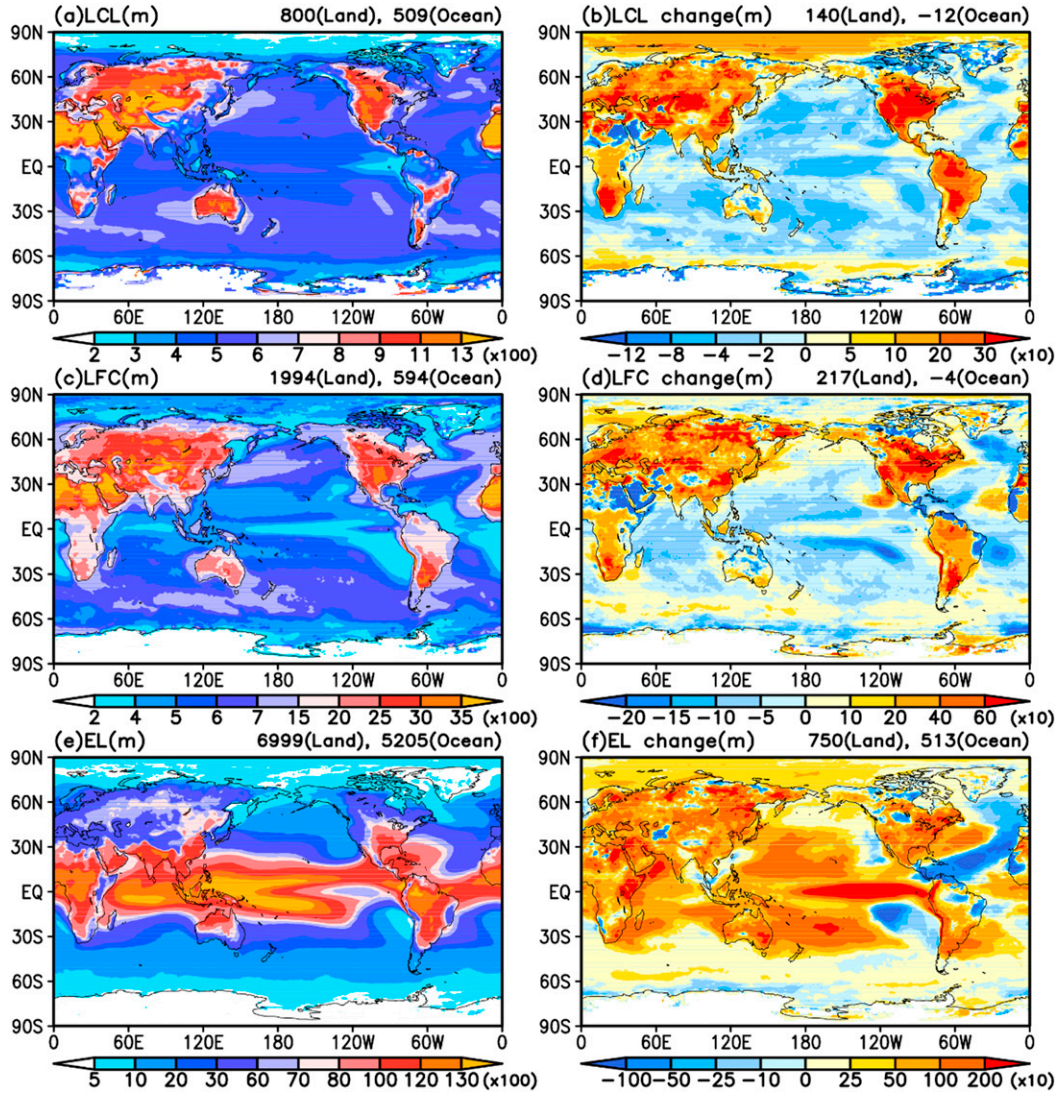

FIG. 13. Distributions of 1995–99 mean annual height of the (a) lifting condensation level (LCL), (c) level of free convection (LFC), and (e) equilibrium level (EL) (in units of 100 m above the lifting level; and (b),(d),(f) their respective changes (in units of 10 m) from 1995–99 to 2095–99 under the RCP8.5 scenario derived using CCSM4 daily data with CAPE = 0 cases excluded. The land and ocean mean values (in units of m) are shown on the top-right corner of each panel.

5. Summary and discussion

In this study, we first examined the present-day CAPE and CIN climatology in CCSM4 using 6-hourly ERA-Interim reanalysis data, and found that the model-simulated CAPE and CIN reasonably capture their mean patterns in the reanalysis. We then analyzed the 6-hourly (and daily) data for the present (1980–99 or 1995–99) and future (2081–2100 or 2095–99) periods simulated by CCSM4 under the RCP8.5 high emissions scenario to quantify the projected atmospheric thermodynamic (i.e., CAPE, CIN, LCL, LFC, EL, and RH) changes and investigate the underlying causes. It is found that indeed CAPE increases everywhere except some subtropical oceans in the future warmer climate, and CIN also becomes stronger (i.e., more negative buoyancy) over most land areas with small changes over the oceans. These mean CAPE and CIN changes result from increased cases with medium-strong CAPE or CIN values but decreased cases with weak CAPE or CIN over land under future warming. These projected changes are broadly consistent with the results from the convection-permitting high-resolution WRF simulations over the United States examined here and also by Rasmussen et al. (2017), which increases our confidence in the CCSM4-projected future changes.

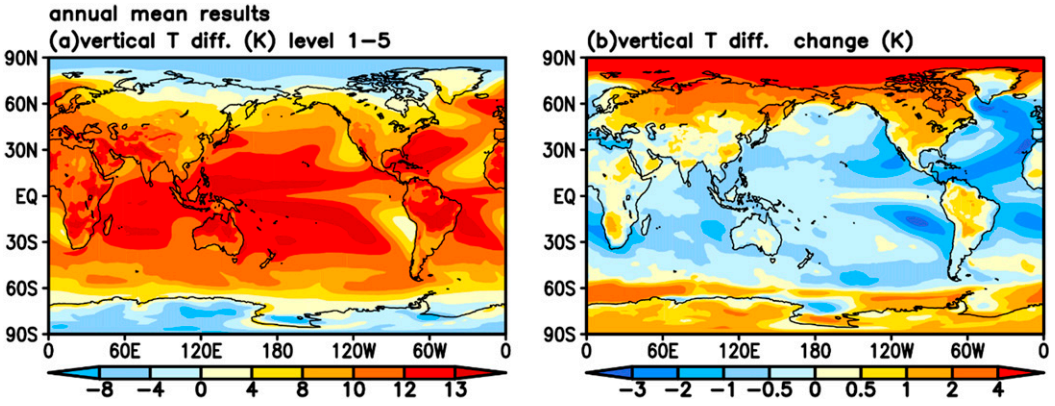

FIG. 14. (a) Distributions of the annual temperature difference between the first (around 978.1 hPa) and fifth (around 776.4 hPa) model levels during 1995–99 and (b) its change from 1995–99 to 2095–99 under the RCP8.5 scenario calculated using CCSM4 daily data.

Calculations with specified changes in air temperature (T) and specific humidity (q) suggest that the CAPE increase results mainly from the effect of increased q, which leads to more condensation and latent heating for the lifted parcel above the LFC, slower cooling as the parcel ascends, and a higher EL, all leading to higher CAPE, while the effect of rising T alone would decrease CAPE. In contrast, the CIN increase results mainly from decreased low-level RH, which leads to higher LCL and higher LFC and thus more negative buoyancy over most land. CIN would weaken over land in a warmer climate without RH changes. Over the oceans, low-level RH increases slightly, leading to some reduction in LCL and LFC and slight weakening of CIN over many tropical oceans. The similar change patterns between the near-surface RH and CIN further suggest an important role of the low-level RH changes for future CIN. Over the subtropical eastern Pacific and Atlantic Ocean, the impact of reduced low-level atmospheric lapse rates dominates over the effect of increased specific humidity, leading to decreased CAPE there.

Our estimates of the relative contributions from the changes in LFC, EL, and lapse rates, all of which result from changes in q and T, indicate that most (>60%) of the CAPE change results from lapse rate changes (including that in the atmosphere and that of the ascending air parcel due to increased q at the lifting level), while the EL change accounts for about 20%–40% of the CAPE change over most of the globe. Over land, the increased LFC leads to about 1%–5% reduction in CAPE but contributes about 5%–20% to the CIN strengthening there. The majority (>80%) of the CIN changes result from the lapse rate changes. Thus, the effects of the q and T changes on CAPE and CIN come mainly through their impacts on the lapse rates of the atmosphere and the ascending parcel.

This land–ocean difference of the low-level RH change may be explained qualitatively as follows. Over ocean, the extra radiative heating from increased GHGs enhances surface evaporation (Held and Soden 2000) which slows down surface warming compared with land, leading to slight RH increases which are energetically constrained (Schneider et al. 2010). Over land, local evaporation is limited by drier top soils (Dai et al. 2018), while the increase in water vapor transport from ocean to land, which accounts for about one-third of land precipitation (Trenberth et al. 2007) and is more important in future warmer climate (Findell et al. 2019), is limited by the slow warming over ocean, which controls the oceanic q increase and thus the amount of water vapor transported to land. The controlling effect of SST warming on changes in q over both land and ocean is also captured in a simple moisture advection model (Chadwick et al. 2016). The drying over land further enhances warming there as more of the GHG-induced radiative heating is used to raise temperature rather than for evaporation, and the enhanced warming leads to more evaporative demand for moisture and thus enhances the aridity further over land, leading to a positive land–atmosphere feedback (Berg et al. 2016). The combination of a fast warming rate and a slow increase in water vapor content (due to water-limited local evaporation and ocean-warming limited ocean-to-land moisture transport) would lead to a RH reduction over land. This physical explanation for the land–ocean contrast in RH changes was confirmed in models using simple constraints based on atmospheric dynamics and moisture transport (Byrne and O'Gorman 2016), which also explains the trends in near-surface temperature and humidity in recent decades (Byrne and O'Gorman 2018).

The increased CIN over land should inhibit the onset of weak-moderate moist convection and allow the CAPE

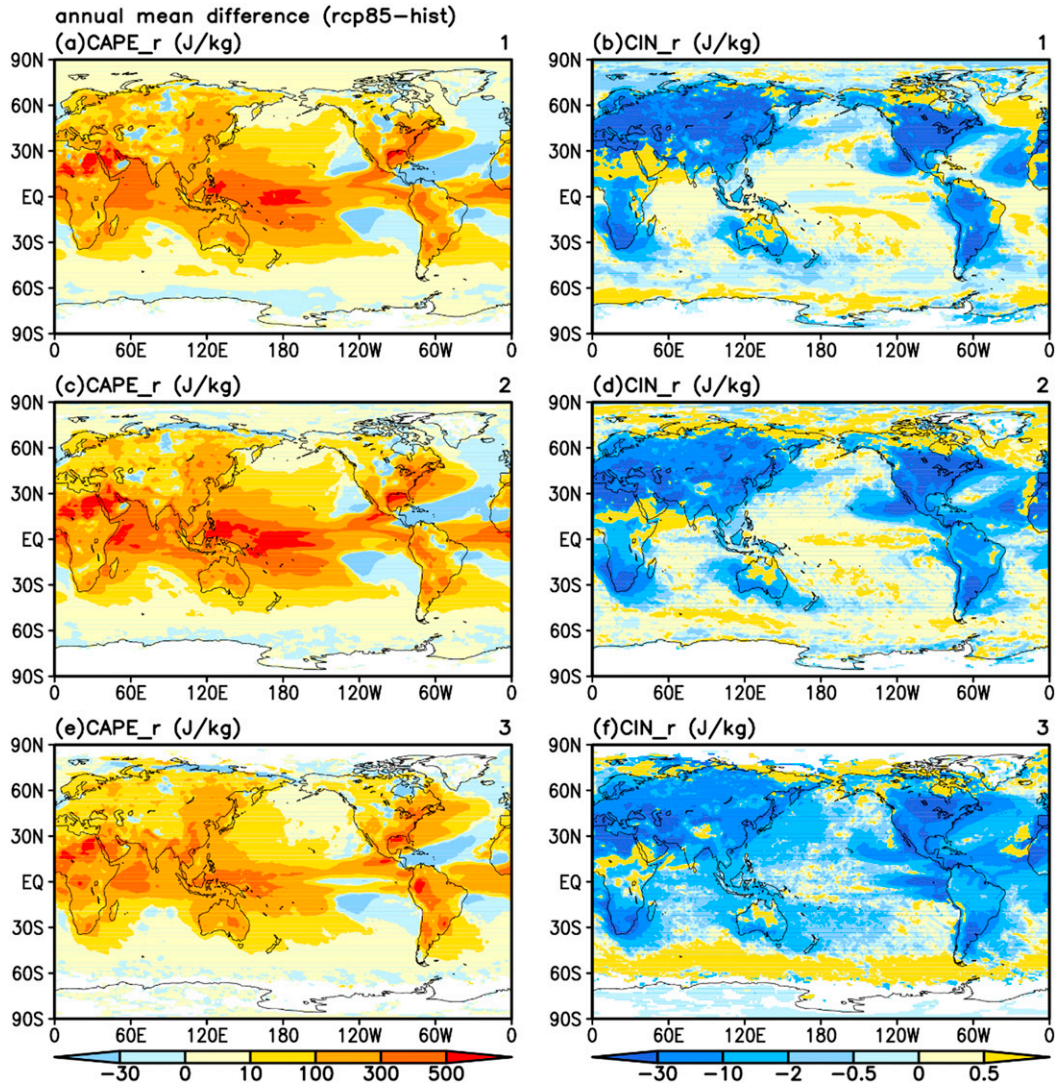

FIG. B1. Distributions of the mean changes in annual (left) CAPE (J kg^{-1}) and (right) CIN (J kg^{-1}) from 1995–99 to 2095–99 under the RCP8.5 scenario with CAPE = 0 cases excluded for a lifting air parcel from the (a),(b) lowest level (i.e., the lowest model level with a hybrid-sigma value of 992.6), (c),(d) second level (with a hybrid-sigma value of 970.6), and (e),(f) third level (with a hybrid-sigma value of 929.6) using CCSM4 daily data.

to build up until intense convection occurs. This process may have also contributed to the projected mean CAPE increase, in addition to the factors discussed above. Such a change also suggests that future moist convection and rainstorms may become less frequent but more intense, which is consistent with previous findings (e.g., Del Genio et al. 2007; Dai et al. 2017). However, how the CAPE and CIN changes are related to future precipitation response to global warming requires further investigation. In particular, the CIN increase over land may help explain the decreasing light-moderate precipitation events under global warming (Shiu et al. 2012; Dai et al. 2017), although such precipitation changes would also occur over oceans (Sun et al. 2007; Dai et al. 2018), where CIN would not strengthen. Another possible link of the CAPE and CIN changes is the association with the increasing seasonal amplitude and variability in near-surface air temperature in the twenty-first century (Chen et al. 2019), as the low-level T affects the buoyancy of the ascending parcel. Further analyses are needed to examine this possible connection.

Acknowledgments. We are very grateful to Editor Dr. Issac Held and three anonymous reviewers for their constructive comments that helped improve the paper considerably. We thank the NCAR modeling groups who made the CCSM4 and WRF-CONUS simulations available to us. Zhang and Chen were supported by the

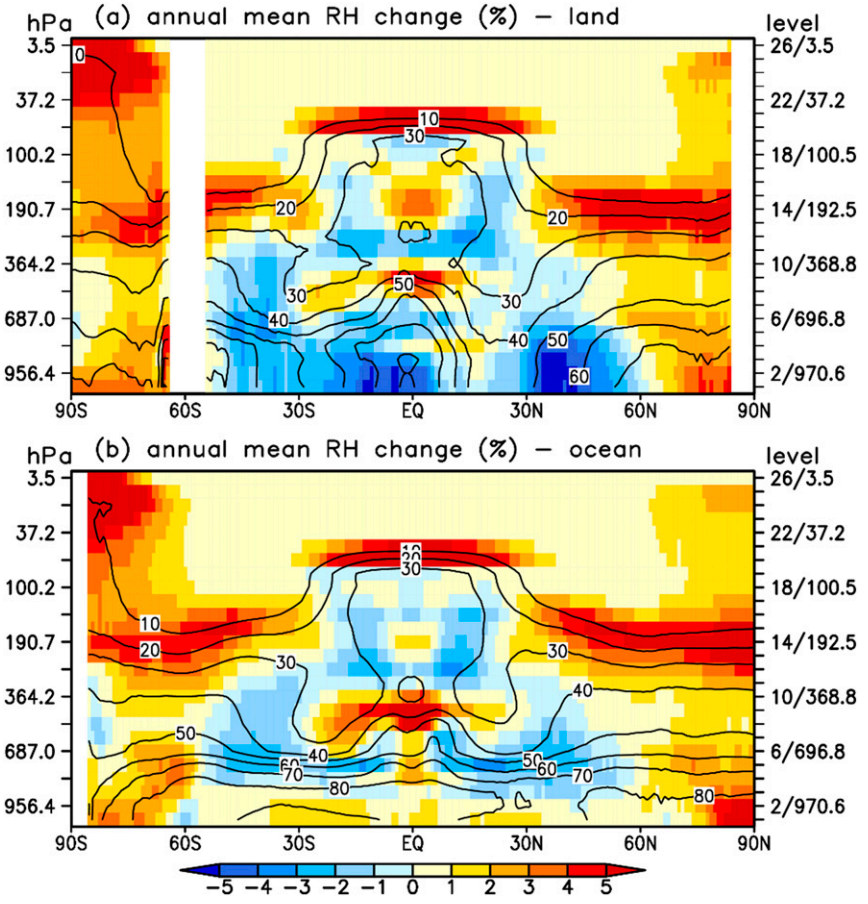

FIG. B2. Latitude–height distributions of zonal-mean annual relative humidity (RH) for 1995–99 (contours; %) and its change (shaded; %) from 1995–99 to 2095–99 under the RCP8.5 scenario averaged over (a) land grid points only and (b) ocean grid points only. The mean pressure averaged over the globe during 1995–99 is shown on the left *y* axis for illustrative purpose; the model levels and corresponding hybrid-sigma values are shown on the right *y* axis.

National Natural Science Foundation of China (41621005, 41575071). Chen also acknowledges the support from the China Scholarship Council to sponsor her visit to the University at Albany. Dai acknowledges the funding support from the U.S. National Science Foundation (Grants AGS-1353740 and OISE-1743738), the U.S. Department of Energy's Office of Science (Award DE-SC0012602), and the U.S. National Oceanic and Atmospheric Administration (Awards NA15OAR4310086 and NA18OAR4310425). Rasmussen acknowledges the support from the U.S. National Science Foundation (Grant AGS-1661657).

APPENDIX A

Calculations of CAPE, CIN, LCL, LFC, and EL

Calculations of T_{vp} are different for the reversible and irreversible process. For the irreversible pseudoadiabat process with all condensed water immediately precipitated out of the parcel, T_{vp} is defined as $T_{vp} = T_p(1 + r_p/\varepsilon)/(1 + r_p)$, where T_p and r_p are the temperature and mixing ratio of the air parcel. For the reversible moist adiabatic process, which keep all the condensates inside the parcel, the density increment due to the liquid or solid water in the parcel should be incorporated into the virtual temperature. In this case, the calculation of T_{vp} becomes $T_{vp} = T_p(1 + r_p/\varepsilon)/(1 + r_p + r_l)$, where r_l is the liquid water mixing ratio (as we assume there is no freezing in our calculations).

We used Espy's equation (Espy 1836; Lawrence 2005) to estimate the height of LCL (h_{LCL}, in units of m): $h_{\mathrm{LCL}} = (T - T_d)/(\gamma_d - \gamma_\tau) \approx 125(T - T_d)$, where T and T_d are temperature and dewpoint temperature at the initial level (in K), γ_d is the dry adiabatic lapse rate ($\approx$9.8 K km^{-1}), and γ_τ is the lapse rate of T_d ($\approx$1.7 K km^{-1}). Based on $e_s(T) = 6.112 \exp[17.67(T - 273.16)/(T - 29.65)]$ and $q = \varepsilon \times e/(p - 0.378e)$, where e_s is the saturated vapor pressure (in hPa) based on Bolton (1980), p is air pressure (in hPa)

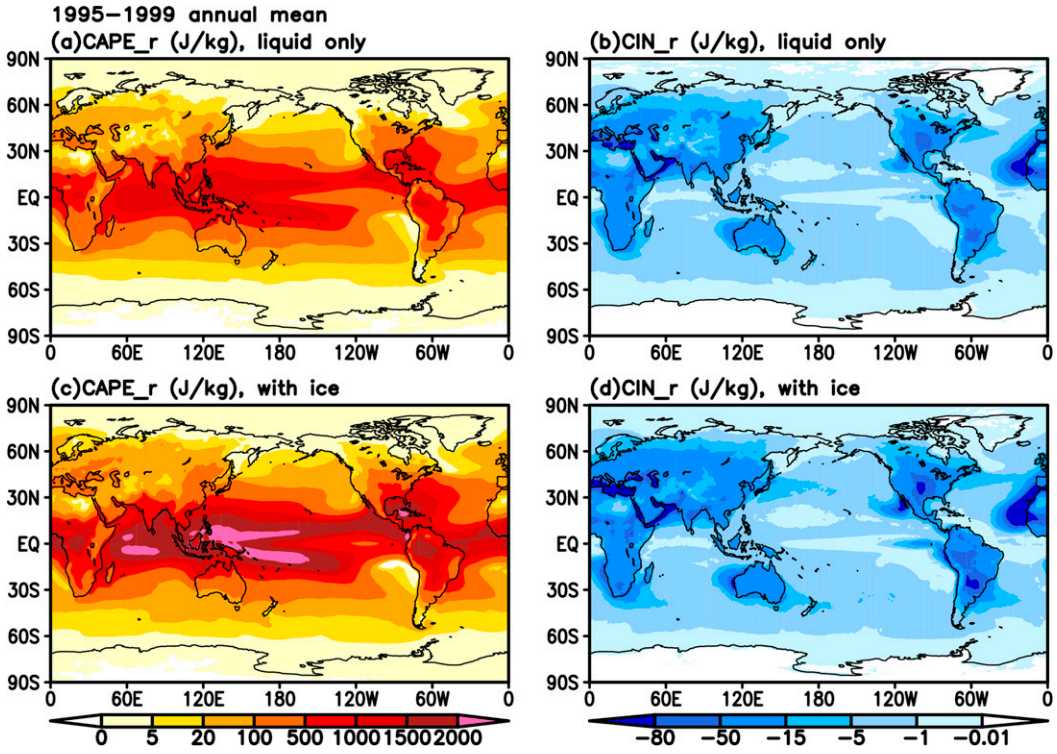

FIG. B3. Distributions of the 1995–99 mean annual (left) CAPE ($J\,kg^{-1}$) and (right) CIN ($J\,kg^{-1}$) calculated under a reversible adiabatic process (a),(b) with no freezing and (c),(d) with freezing (i.e., accounting for the latent heat of fusion) for a parcel lifted from the lowest model level with a hybrid-sigma value of 992.6 using daily data from CCSM4 historical simulation. The CAPE integration stops at the 15th model level (~162 hPa).

and q is specific humidity (in $g\,g^{-1}$), taking $e = e_s(T_d)$, we can obtain T_d at the initial level from p and q, and then calculate the h_{LCL}.

We used the hypsometric equation (Wallace and Hobbs 1977) $z_2 - z_1 = R_d\overline{T_v}/g \times \ln(p_1/p_2)$ to obtain the approximate height in meters above the ground for LFC and EL from their pressure levels. At each grid, p_1 and p_2 (z_1 and z_2) are the pressure (height) of two adjacent model levels and $\overline{T_v}$ is the mean T_v between the two levels.

APPENDIX B

Sensitivity to Different Lifting Levels and the Effect of Freezing

CAPE and CIN values are sensitive to different calculation algorithms, such as the choices of the lifting level, parcel path (i.e., reversible versus irreversible), and virtual temperature corrections. Besides calculating them using both reversible and irreversible paths, we have conducted some other tests using daily CCSM4 data to test the robustness of our conclusions. When lifting the air parcel from the lowest three levels separately with the integration ending at the same 15th model level, mean CAPE and CIN show similar patterns over the globe with weaker CAPE and CIN for a higher lifting level (not shown). The corresponding changes in CAPE and CIN also show similar distributions with some differences in magnitude (Fig. B1) except for enhanced CIN over many ocean areas when lifting from the third level (Fig. B1f), which is related to the decreased RH at this level (Fig. B2). Different lifting levels also affect the mean value of the three height parameters (i.e., LCL, LFC, and EL) related to the CAPE and CIN calculation, while their changes are comparable (not shown). For example, the higher LFC and lower EL over the tropical oceans when lifting the parcel from the third level are spatially correlated with the weaker CAPE there, while the LFC change becomes positive over many low-latitude oceans when lifting the parcel from the third level and it is consistent with the enhanced CIN there (Fig. B1f). Craven et al. (2002) noticed that the LCL heights calculated using surface-based parcels are smaller than those using the lowest 100-hPa mean-layer parcels (due to the higher RH near the surface), which influences the CAPE and CIN calculations. Thus, the magnitudes of the mean CAPE and CIN and their changes will differ somewhat if the

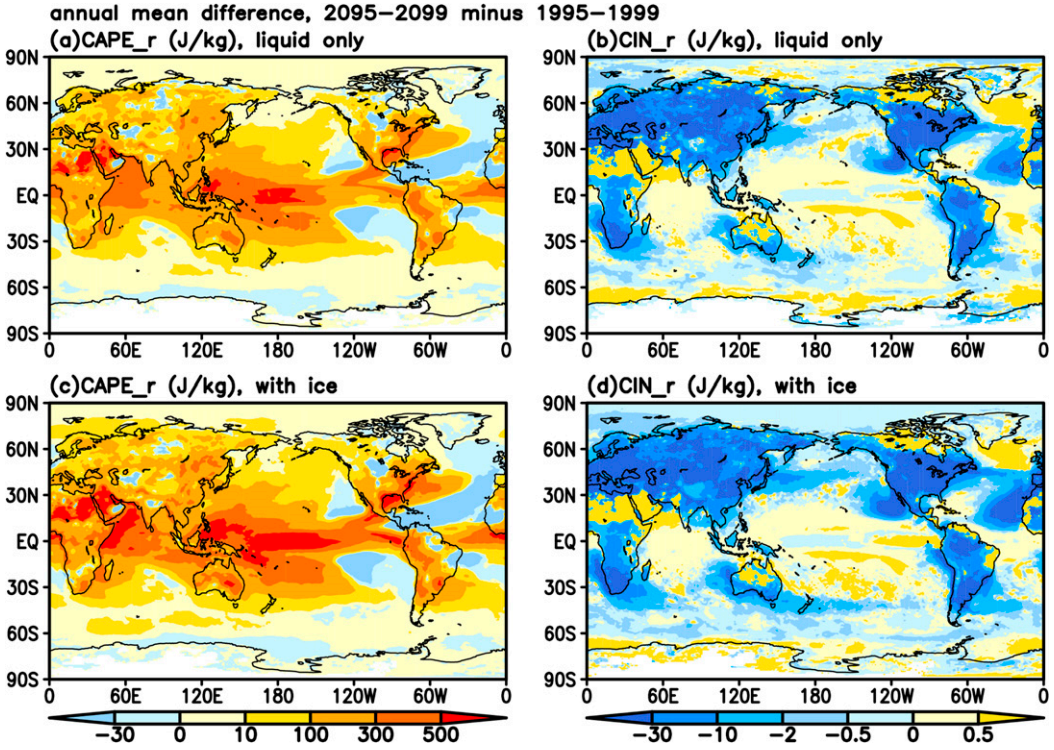

FIG. B4. Distributions of the changes in annual (left) CAPE (J kg^{-1}) and (right) CIN (J kg^{-1}) under a reversible adiabatic process (a),(b) without freezing and (c),(d) with freezing from 1995–99 to 2095–99 with the CAPE = 0 cases excluded under the RCP8.5 scenario calculated using CCSM4 daily data.

parcel is lifted from a higher level than the first level used here, but the general conclusions regarding the CAPE and CIN changes should be similar as long as the lifting level is still within the lower ~100-hPa layer (i.e., the boundary layer), within which RH shows similar changes (Fig. B2).

More tests were also conducted, such as changing the integration stopping level to the 16th and 17th model level from the 15th level used in the above, as the 15th level might be lower than the actual EL for some locations. Larger CAPE values with higher EL and larger changes were found mainly over tropical oceans for a higher stopping level (not shown), which would only enhance the CAPE increase discussed above but would not affect our conclusions. In summary, these tests of changing the lifting level and integration stopping level show that increased CAPE over most of the globe and enhanced CIN over land are a robust feature in a future warmer climate, while weakened CIN over ocean areas is valid only when lifting the parcel within the boundary layer because the increased RH only exists there (Fig. B2b).

In the above CAPE and CIN calculations, we have neglected the latent heat of fusion from the freezing of the condensed water above the freezing height, which is suggested to be responsible for much of the CAPE values under the reversible adiabatic process over the tropical oceans (Williams and Renno 1993). Clearly, this impact is at maximum for the reversible moist adiabatic process and does not exist for the irreversible pseudoadiabatic process as all the condensates would immediately fall out of the air parcel in this case. The reality is likely somewhere between these two cases. To provide some estimates of this impact, we did some tests through calculating CAPE and CIN with and without accounting for the latent heat of fusion from freezing using daily CCSM4 data under the reversible adiabatic process (thus, it represents the maximum possible impact). The mean CAPE and CIN for 1995–99 for the no-freezing case calculated using daily data (Figs. B3a,b) are very similar to those calculated using 6-hourly data (Figs. 2c,d). Thus, we expect the comparison in Figs. B3 and B4 between the no-freezing and freezing cases to be similar if 6-hourly data were used. Figure B3 shows that indeed including the latent heat of fusion increases the mean CAPE substantially over the low-latitude oceans. This results from increased buoyancy above the LFC and a higher EL when freezing is considered. However, the future CAPE and CIN change patterns are very similar for the two cases, besides the larger CAPE increases over the tropical oceans in the freezing case

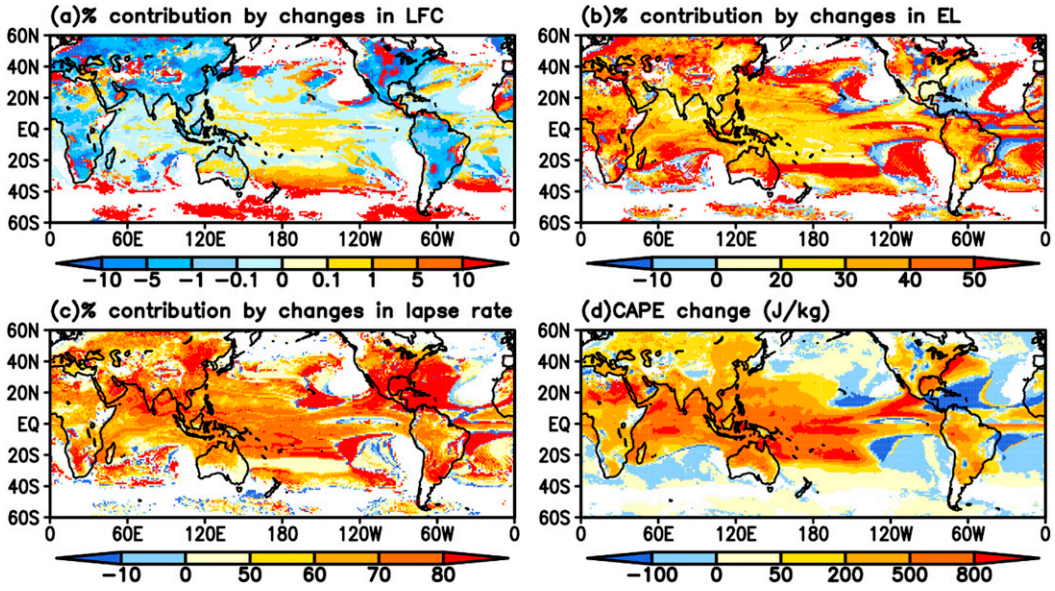

FIG. C1. Percentage contributions to (d) local CAPE change (J kg^{-1}) from 1995–99 to 2095–99 from changes in (a) LFC, (b) EL, and (c) lapse rates (including the q change at the lifting level) estimated using summer (JJA for Northern Hemisphere and DJF for Southern Hemisphere) mean T and q profiles during 1995–99 and 2095–99. The buoyancy profiles on CCSM4's original model levels were interpolated onto a set of 10 hPa-interval pressure levels before calculating the contributions (see appendix C for more details). When the CAPE change is negative (i.e., over the western Atlantic), the positive contribution ratio indicates that this factor contributes to the CAPE decrease. The uncolored areas indicate that the mean T and q profiles are under the absolute stable situation (mostly over mid- to high latitudes) or the CAPE change is smaller than 1.0 J kg^{-1}. The calculations excluded daily CAPE = 0 cases in computing the mean T and q profiles.

(Fig. B4). Thus, neglecting freezing should not affect our conclusions.

APPENDIX C

Estimates of the Individual Contributions to CAPE and CIN Changes

Ideally, in section 4c one would like to know the quantitative contribution by each of the factors (i.e., changes in the LFC, EL, and lapse rates) to the CAPE or CIN changes. However, the LFC and EL levels vary with individual T and q profiles, which also determine the lapse rates of the environment and of the ascending parcel. This means that these three factors are tightly coupled and thus we cannot just change one of them while fixing the other two in our CAPE and CIN calculations. Furthermore, it is hard to find a reference basis from today's climate for calculating the CAPE and CIN changes for individual T and q profiles, which contain large unforced internal variations. Because of these issues, it is difficult to perform a precise calculation of the individual contributions using daily or 6-hourly T and q profiles.

To provide an approximate estimate of the individual contributions, we used the multiyear mean T and q profiles (and their corresponding LFC and EL levels) from current and future climates and following the approach suggested by one of the reviewers of the manuscript: 1) Use current mean T and q profiles to estimate the positive buoyancy between present-day LFC and future LFC (which generally increases from today's LFC) and use this estimate as the contribution of the LFC change to the total CAPE change; 2) use future mean T and q profiles to estimate the positive buoyancy between present-day EL and future EL (which generally increases from today's EL) and use this estimate as the contribution of the EL change to the total CAPE change; and 3) the residual CAPE change after subtracting the LFC's and EL's contributions is considered as the contribution from lapse rate changes, which include the changes in the lapse rate of the environment (i.e., the atmospheric lapse rate) and in the lapse rate of the ascending parcel that is determined primarily by q and T at the lifting level (cf. Fig. 1). Since we use future T and q profiles in estimating the EL's contribution as today's T and q profiles would not yield positive buoyancy above today's EL, this estimate would also include some contribution from the changed lapse rates above today's EL. For some locations where future LFC (EL) decreases, then the future (current) mean T and q

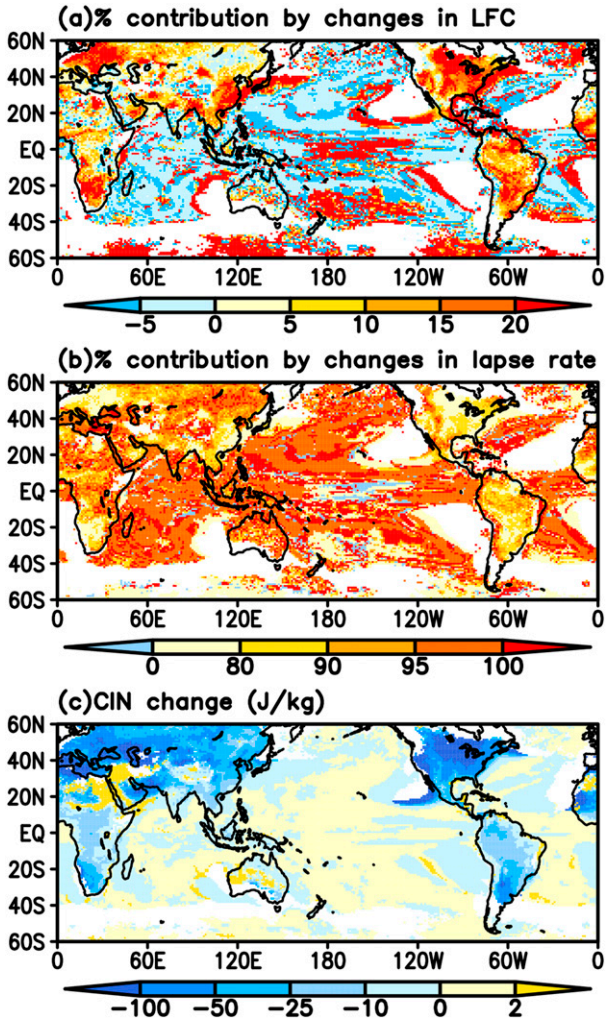

FIG. C2. As in Fig. C1, but for the contributions to (c) local CIN change (J kg^{-1}) from changes in (a) LFC and (b) lapse rates (including the q change at the lifting level). When the CIN change is negative (e.g., over most land areas), a positive contribution indicates that this factor contributes to the CIN strengthening (i.e., larger negative CIN). When the CIN change is positive (i.e., over most ocean areas), a positive contribution indicates that this factor contributes to the CIN weakening (i.e., smaller negative CIN). The uncolored areas indicate that the mean T and q profiles are under the absolute stable situation (mostly over mid- to high latitudes) or the CIN change is smaller than 0.001 J kg^{-1}.

profiles would be used to estimate its contribution to the CAPE change.

For estimating the contribution from the LFC increase to the total CIN change, we use the future mean T and q profiles to estimate the negative buoyancy between the current LFC and the higher future LFC and use this estimate as the contribution by the LFC change to the total CIN change. The residual CIN change after removing the LFC's contribution is considered as the contribution by the lapse rate changes. If future LFC decreases at some locations, then the current mean T and q profiles are used.

The results from these calculations are shown in Figs. C1 and C2. Figure C1 shows that most (>60%) of the CAPE change results from the lapse rate changes, while the EL increase contributes about 20%–40% to the CAPE change over most of the globe. The increased LFC leads to 1%–5% reduction in CAPE over most land but contributes little over the oceans. For the CIN change, even a larger percentage (>80%) results from the lapse rate changes, with the LFC change contributing only about 5%–20% over land (Fig. C2).

REFERENCES

Adams, D. K., and E. P. Souza, 2009: CAPE and convective events in the Southwest during the North American monsoon. *Mon. Wea. Rev.*, **137**, 83–98, https://doi.org/10.1175/2008MWR2502.1.

Allen, J. T., D. J. Karoly, and K. J. Walsh, 2014: Future Australian severe thunderstorm environments. Part II: The influence of a strongly warming climate on convective environments. *J. Climate*, **27**, 3848–3868, https://doi.org/10.1175/JCLI-D-13-00426.1.

Berg, A., and Coauthors, 2016: Land–atmosphere feedbacks amplify aridity increase over land under global warming. *Nat. Climate Change*, **6**, 869–874, https://doi.org/10.1038/nclimate3029.

Bolton, D., 1980: Computation of equivalent potential temperature. *Mon. Wea. Rev.*, **108**, 1046–1053, https://doi.org/10.1175/1520-0493(1980)108<1046:TCOEPT>2.0.CO;2.

Brooks, H. E., 2013: Severe thunderstorms and climate change. *Atmos. Res.*, **123**, 129–138, https://doi.org/10.1016/j.atmosres.2012.04.002.

Byrne, M. P., and P. A. O'Gorman, 2016: Understanding decreases in land relative humidity with global warming: Conceptual model and GCM simulations. *J. Climate*, **29**, 9045–9061, https://doi.org/10.1175/JCLI-D-16-0351.1.

——, and ——, 2018: Trends in continental temperature and humidity directly linked to ocean warming. *Proc. Natl. Acad. Sci. USA*, **115**, 4863–4868, https://doi.org/10.1073/pnas.1722312115.

Carlson, T. N., S. G. Benjamin, G. S. Forbes, and Y.-F. Li, 1983: Elevated mixed layers in the regional severe storm environment: Conceptual model and case studies. *Mon. Wea. Rev.*, **111**, 1453–1474, https://doi.org/10.1175/1520-0493(1983)111<1453:EMLITR>2.0.CO;2.

Chadwick, R., P. Good, and K. Willett, 2016: A simple moisture advection model of specific humidity change over land in response to SST warming. *J. Climate*, **29**, 7613–7632, https://doi.org/10.1175/JCLI-D-16-0241.1.

Chen, D., and A. Dai, 2018: Dependence of estimated precipitation frequency and intensity on data resolution. *Climate Dyn.*, **50**, 3625–3647, https://doi.org/10.1007/s00382-017-3830-7.

Chen, J., A. Dai, and Y. Zhang, 2019: Projected changes in daily variability and seasonal cycle of near-surface air temperature over the globe during the twenty-first century. *J. Climate*, **32**, 8537–8561, https://doi.org/10.1175/JCLI-D-19-0438.1.

Craven, J. P., R. E. Jewell, and H. E. Brooks, 2002: Comparison between observed convective cloud-base heights and lifting condensation level for two different lifted parcels. *Wea. Forecasting*, **17**, 885–890, https://doi.org/10.1175/1520-0434(2002)017<0885:CBOCCB>2.0.CO;2.

Dai, A., F. Giorgi, and K. E. Trenberth, 1999: Observed and model-simulated precipitation diurnal cycle over the contiguous United

States. *J. Geophys. Res.*, **104**, 6377–6402, https://doi.org/10.1029/98JD02720.

——, J. Wang, P. W. Thorne, D. E. Parker, L. Haimberger, and X. L. Wang, 2011: A new approach to homogenize daily radiosonde humidity data. *J. Climate*, **24**, 965–991, https://doi.org/10.1175/2010JCLI3816.1.

——, R. M. Rasmussen, C. Liu, K. Ikeda, and A. F. Prein, 2017: A new mechanism for warm-season precipitation response to global warming based on convection-permitting simulations. *Climate Dyn.*, https://doi.org/10.1007/s00382-017-3787-6.

——, T. Zhao, and J. Chen, 2018: Climate change and drought: A precipitation and evaporation perspective. *Curr. Climate Change Rep.*, **4**, 301–312, https://doi.org/10.1007/s40641-018-0101-6.

——, D. Luo, M. Song, and J. Liu, 2019: Arctic amplification is caused by sea-ice loss under increasing CO_2. *Nat. Commun.*, **10**, 121, https://doi.org/10.1038/s41467-018-07954-9.

Dee, D. P., and Coauthors, 2011: The ERA-Interim reanalysis: Configuration and performance of the data assimilation system. *Quart. J. Roy. Meteor. Soc.*, **137**, 553–597, https://doi.org/10.1002/qj.828.

Del Genio, A. D., M.-S. Yao, and J. Jonas, 2007: Will moist convection be stronger in a warmer climate? *Geophys. Res. Lett.*, **34**, L16703, https://doi.org/10.1029/2007GL030525.

DeMott, C. A., and D. A. Randall, 2004: Observed variations of tropical convective available potential energy. *J. Geophys. Res.*, **109**, D02102, https://doi.org/10.1029/2003JD003784.

Diffenbaugh, N. S., M. Scherer, and R. J. Trapp, 2013: Robust increases in severe thunderstorm environments in response to greenhouse forcing. *Proc. Natl. Acad. Sci. USA*, **110**, 16 361–16 366, https://doi.org/10.1073/pnas.1307758110.

Doswell, C. A., III, and E. N. Rasmussen, 1994: The effect of neglecting the virtual temperature correction on CAPE calculations. *Wea. Forecasting*, **9**, 625–629, https://doi.org/10.1175/1520-0434(1994)009<0625:TEONTV>2.0.CO;2.

ECMWF, 2011: ERA-Interim. Accessed 1 December 2018, https://www.ecmwf.int/en/forecasts/datasets/reanalysis-datasets/era-interim.

Eltahir, E. A., and J. S. Pal, 1996: Relationship between surface conditions and subsequent rainfall in convective storms. *J. Geophys. Res.*, **101**, 26 237–26 245, https://doi.org/10.1029/96JD01380.

Emanuel, K. A., 1994: *Atmospheric Convection*. Oxford University Press, 580 pp.

——, J. D. Neelin, and C. S. Bretherton, 1994: On large-scale circulations in convecting atmospheres. *Quart. J. Roy. Meteor. Soc.*, **120**, 1111–1143, https://doi.org/10.1002/qj.49712051902.

Espy, J. P., 1836: Essays on meteorology, No. IV: North east storms, volcanoes, and columnar clouds. *J. Franklin Inst.*, **22**, 239–246, https://doi.org/10.1016/S0016-0032(36)91215-2.

Findell, K. L., P. W. Keys, R. J. van der Ent, B. R. Lintner, A. Berg, and J. P. Krasting, 2019: Rising temperatures increase importance of oceanic evaporation as a source for continental precipitation. *J. Climate*, **32**, 7713–7726, https://doi.org/10.1175/JCLI-D-19-0145.1.

Fovell, R. G., 1991: Influence of the Coriolis force on two-dimensional model storms. *Mon. Wea. Rev.*, **119**, 606–630, https://doi.org/10.1175/1520-0493(1991)119<0606:IOTCFO>2.0.CO;2.

Gent, P. R., and Coauthors, 2011: The Community Climate System Model version 4. *J. Climate*, **24**, 4973–4991, https://doi.org/10.1175/2011JCLI4083.1.

Gettelman, A., D. J. Seidel, M. C. Wheeler, and R. J. Ross, 2002: Multidecadal trends in tropical convective available potential energy. *J. Geophys. Res.*, **107**, 4606, https://doi.org/10.1029/2001JD001082.

Held, I. M., and B. J. Soden, 2000: Water vapor feedback and global warming. *Annu. Rev. Energy Environ.*, **25**, 441–475, https://doi.org/10.1146/annurev.energy.25.1.441.

Holley, D. M., S. R. Dorling, C. J. Steele, and N. Earl, 2014: A climatology of convective available potential energy in Great Britain. *Int. J. Climatol.*, **34**, 3811–3824, https://doi.org/10.1002/joc.3976.

Houze, R. A., Jr., D. C. Wilton, and B. F. Smull, 2007: Monsoon convection in the Himalayan region as seen by the TRMM Precipitation Radar. *Quart. J. Roy. Meteor. Soc.*, **133**, 1389–1411, https://doi.org/10.1002/qj.106.

Lawrence, M. G., 2005: The relationship between relative humidity and the dewpoint temperature in moist air: A simple conversion and applications. *Bull. Amer. Meteor. Soc.*, **86**, 225–234, https://doi.org/10.1175/BAMS-86-2-225.

Liu, C., and Coauthors, 2017: Continental-scale convection-permitting modeling of the current and future climate of North America. *Climate Dyn.*, **49**, 71–95, https://doi.org/10.1007/s00382-016-3327-9.

Meukaleuni, C., A. Lenouo, and D. Monkam, 2016: Climatology of convective available potential energy (CAPE) in ERA-Interim reanalysis over West Africa. *Atmos. Sci. Lett.*, **17**, 65–70, https://doi.org/10.1002/asl.601.

Muller, C. J., P. A. O'Gorman, and L. E. Back, 2011: Intensification of precipitation extremes with warming in a cloud-resolving model. *J. Climate*, **24**, 2784–2800, https://doi.org/10.1175/2011JCLI3876.1.

Murugavel, P., S. D. Pawar, and V. Gopalakrishnan, 2012: Trends of convective available potential energy over the Indian region and its effect on rainfall. *Int. J. Climatol.*, **32**, 1362–1372, https://doi.org/10.1002/joc.2359.

Myoung, B., and J. W. Nielsen-Gammon, 2010: Sensitivity of monthly convective precipitation to environmental conditions. *J. Climate*, **23**, 166–188, https://doi.org/10.1175/2009JCLI2792.1.

Parker, D. J., 2002: The response of CAPE and CIN to tropospheric thermal variations. *Quart. J. Roy. Meteor. Soc.*, **128**, 119–130, https://doi.org/10.1256/00359000260498815.

Rasmussen, K. L., and R. A. Houze Jr., 2011: Orogenic convection in subtropical South America as seen by the TRMM satellite. *Mon. Wea. Rev.*, **139**, 2399–2420, https://doi.org/10.1175/MWR-D-10-05006.1.

——, and ——, 2016: Convective initiation near the Andes in subtropical South America. *Mon. Wea. Rev.*, **144**, 2351–2374, https://doi.org/10.1175/MWR-D-15-0058.1.

——, A. F. Prein, R. M. Rasmussen, K. Ikeda, and C. Liu, 2017: Changes in the convective population and thermodynamic environments in convection-permitting regional climate simulations over the United States. *Climate Dyn.*, https://doi.org/10.1007/s00382-017-4000-7.

Riemann-Campe, K., K. Fraedrich, and F. Lunkeit, 2009: Global climatology of convective available potential energy (CAPE) and convective inhibition (CIN) in ERA-40 reanalysis. *Atmos. Res.*, **93**, 534–545, https://doi.org/10.1016/j.atmosres.2008.09.037.

Romps, D. M., 2011: Response of tropical precipitation to global warming. *J. Atmos. Sci.*, **68**, 123–138, https://doi.org/10.1175/2010JAS3542.1.

——, 2014: An analytical model for tropical relative humidity. *J. Climate*, **27**, 7432–7449, https://doi.org/10.1175/JCLI-D-14-00255.1.

——, 2016: Clausius–Clapeyron scaling of CAPE from analytical solutions to RCE. *J. Atmos. Sci.*, **73**, 3719–3737, https://doi.org/10.1175/JAS-D-15-0327.1.

Schneider, T., P. A. O'Gorman, and X. J. Levine, 2010: Water vapor and the dynamics of climate changes. *Rev. Geophys.*, **48**, RG3001, https://doi.org/10.1029/2009RG000302.

Seeley, J. T., and D. M. Romps, 2015a: The effect of global warming on severe thunderstorms in the United States. *J. Climate*, **28**, 2443–2458, https://doi.org/10.1175/JCLI-D-14-00382.1.

——, and ——, 2015b: Why does tropical convective available potential energy (CAPE) increase with warming? *Geophys. Res. Lett.*, **42**, 10 429–10 437, https://doi.org/10.1002/2015GL066199.

Shiu, C. J., S. C. Liu, C. Fu, A. Dai, and Y. Sun, 2012: How much do precipitation extremes change in a warming climate? *Geophys. Res. Lett.*, **39**, L17707, https://doi.org/10.1029/2012GL052762.

Simmons, A. J., K. M. Willett, P. D. Jones, P. W. Thorne, and D. P. Dee, 2010: Low-frequency variations in surface atmospheric humidity, temperature, and precipitation: Inferences from reanalyses and monthly gridded observational data sets. *J. Geophys. Res.*, **115**, D01110, https://doi.org/10.1029/2009JD012442.

Singh, M. S., and P. A. O'Gorman, 2013: Influence of entrainment on the thermal stratification in simulations of radiative-convective equilibrium. *Geophys. Res. Lett.*, **40**, 4398–4403, https://doi.org/10.1002/grl.50796.

——, Z. Kuang, E. D. Maloney, W. M. Hannah, and B. O. Wolding, 2017: Increasing potential for intense tropical and subtropical thunderstorms under global warming. *Proc. Natl. Acad. Sci. USA*, **114**, 11 657–11 662, https://doi.org/10.1073/pnas.1707603114.

Sobel, A. H., and S. J. Camargo, 2011: Projected future seasonal changes in tropical summer climate. *J. Climate*, **24**, 473–487, https://doi.org/10.1175/2010JCLI3748.1.

Sun, Y., S. Solomon, A. Dai, and R. Portmann, 2007: How often will it rain? *J. Climate*, **20**, 4801–4818, https://doi.org/10.1175/JCLI4263.1.

Taylor, K. E., R. J. Stouffer, and G. A. Meehl, 2012: An overview of CMIP5 and the experiment design. *Bull. Amer. Meteor. Soc.*, **93**, 485–498, https://doi.org/10.1175/BAMS-D-11-00094.1.

Tompkins, A. M., 2001: Organization of tropical convection in low vertical wind shears: The role of water vapor. *J. Atmos. Sci.*, **58**, 529–545, https://doi.org/10.1175/1520-0469(2001)058<0529:OOTCIL>2.0.CO;2.

Trapp, R. J., N. S. Diffenbaugh, H. E. Brooks, M. E. Baldwin, E. D. Robinson, and J. S. Pal, 2007: Changes in severe thunderstorm environment frequency during the 21st century due to anthropogenically enhanced global radiative forcing. *Proc. Natl. Acad. Sci. USA*, **104**, 19 719–19 723, https://doi.org/10.1073/pnas.0705494104.

Trenberth, K. E., A. Dai, R. M. Rasmussen, and D. B. Parsons, 2003: The changing character of precipitation. *Bull. Amer. Meteor. Soc.*, **84**, 1205–1218, https://doi.org/10.1175/BAMS-84-9-1205.

——, L. Smith, T. Qian, A. Dai, and J. Fasullo, 2007: Estimates of the global water budget and its annual cycle using observational and model data. *J. Hydrometeor.*, **8**, 758–769, https://doi.org/10.1175/JHM600.1.

Van Klooster, S. L., and P. J. Roebber, 2009: Surface-based convective potential in the contiguous United States in a business-as-usual future climate. *J. Climate*, **22**, 3317–3330, https://doi.org/10.1175/2009JCLI2697.1.

Wallace, J. M., and R. V. Hobbs, 1977: *Atmospheric Science: An Introductory Survey*. Academic Press, 467 pp.

Williams, E., 1991: Comments on "Thunderstorms above frontal surfaces in environments without positive CAPE. Part I: A climatology." *Mon. Wea. Rev.*, **119**, 2511–2513, https://doi.org/10.1175/1520-0493(1991)119<2511:COAFSI>2.0.CO;2.

——, and N. Renno, 1993: An analysis of the conditional instability of the tropical atmosphere. *Mon. Wea. Rev.*, **121**, 21–36, https://doi.org/10.1175/1520-0493(1993)121<0021:AAOTCI>2.0.CO;2.

Ye, B., A. D. Del Genio, and K. K. Lo, 1998: CAPE variations in the current climate and in a climate change. *J. Climate*, **11**, 1997–2015, https://doi.org/10.1175/1520-0442-11.8.1997.

Yin, J., J. D. Albertson, J. R. Rigby, and A. Porporato, 2015: Land and atmospheric controls on initiation and intensity of moist convection: CAPE dynamics and LCL crossings. *Water Resour. Res.*, **51**, 8476–8493, https://doi.org/10.1002/2015WR017286.

Zhang, G. J., 2002: Convective quasi-equilibrium in midlatitude continental environment and its effect on convective parameterization. *J. Geophys. Res.*, **107**, 4220, https://doi.org/10.1029/2001JD001005.

——, and N. A. McFarlane, 1991: Convective stabilization in midlatitudes. *Mon. Wea. Rev.*, **119**, 1915–1928, https://doi.org/10.1175/1520-0493(1991)119<1915:CSIM>2.0.CO;2.

Zipser, E. J., D. J. Cecil, C. Liu, S. W. Nesbitt, and D. P. Yorty, 2006: Where are the most intense thunderstorms on Earth? *Bull. Amer. Meteor. Soc.*, **87**, 1057–1072, https://doi.org/10.1175/BAMS-87-8-1057.